

## Development of an SPH-based numerical wave–current tank and application to wave energy converters

Salvatore Capasso <sup>a,\*</sup>, Bonaventura Tagliafierro <sup>b,c,d</sup>, Iván Martínez-Estévez <sup>e</sup>, Corrado Altomare <sup>c</sup>, Moncho Gómez-Gesteira <sup>e</sup>, Malin Götteman <sup>b</sup>, Giacomo Viccione <sup>a</sup>

<sup>a</sup> Environmental and Maritime Hydraulics Laboratory, University of Salerno, Fisciano, SA, Italy

<sup>b</sup> Department of Electrical Engineering, Uppsala University, Uppsala, Sweden

<sup>c</sup> Universitat Politècnica de Catalunya – BarcelonaTech, Barcelona, Spain

<sup>d</sup> School of Natural and Built Environment, Queen's University Belfast, Northern Ireland, Belfast, United Kingdom

<sup>e</sup> Environmental Physics Laboratory, CIM-UVIGO, Universidade de Vigo, Ourense, Spain

### ARTICLE INFO

#### Keywords:

Waves and current  
DualSPHysics  
Point-absorber  
Numerical wave tank  
Floating structures

### ABSTRACT

This research proposes a high-fidelity based numerical tank designed to analyze the modified hydrodynamics that develops in waves–current fields, aimed at generating power matrices for wave energy converters (WEC). This tank is developed within the open source DualSPHysics Lagrangian framework using the Smoothed Particle Hydrodynamics (SPH) method, validated with physical data, and applied to simulate a point-absorber WEC. Our proposed numerical facility implements open boundary conditions, employing third-order consistent wave theory for direct generation, with flow field constrained by a Doppler correlation function. Reference data is collected from dedicated physical tests for monochromatic waves; the wave–current numerical basin demonstrates very high accuracy in terms of wave transformation and velocity field. In the second segment of this paper, a current-aware power transfer function is computed for the taut-moored point-absorber Uppsala University WEC (UUWEC). Parametrically defined regular waves with uniform currents are utilized to map an operational sea state featuring currents of different directions and intensities. In terms of power capture capabilities, the modified dynamics observed in presence of currents translates in a dependence of the WEC's power matrix not only on wave parameters, but also on current layouts. The UUWEC's power output has revealed that regardless of current directionality, annual output consistently decreases, with a registered power drop as high as 10% when an expected current field is introduced.

### 1. Introduction

In the context of the green energy transition, engineers and designers are expected to contribute with efficient and sustainable solutions, fostering untapped resources. To cope with the growing energy demand and diversify the available energy mix, the marine renewable energy pool [1,2] is a promising asset to be targeted in the short-medium term [3,4]. Marine renewable energy deployment, however, comes with many uncertainties and challenges [5,6], due to a relative lack of experience on the behavior of novel, cutting-edge (and costly) technologies in hostile environments [7–10]. Within the offshore renewable energy (ORE) family, moored floating structures [11] for energy harvesting proved, with costly failures, that present design methods may fail to meet demand if they do not take into account the fully coupled wave–structure interaction (WSI) phenomena, thus ignoring higher-order effects [12–15]. Both wave energy converters (WECs) and floating offshore wind turbines (FOWTs), despite having

different target behaviors or degree of technological readiness, are still facing issues as such.

High-end numerical simulations constitute a valid and well-established support to address WSI, and are gaining credibility even when not directly supported by physical campaigns. When it comes to reproducing harsh environmental conditions or extreme actions, computational fluid dynamics (CFD) methods can overcome some of the restrictive hypotheses of linear, weakly nonlinear, or fully nonlinear potential flow-based solvers (see [16] for WECs or [17] for FOWTs). Therefore, the use of CFD is most suitable when the ocean environment features complex hydrodynamics, which may also develop from the combination of different physical phenomena.

The latter record certainly includes the combination of waves and currents, often not negligible in eyed sites for offshore energy deployment. Ocean-, tidal- or wind-generated currents, with their typical features, interact with wave patterns producing unique and complex

\* Corresponding author.

E-mail address: [scapasso@unisa.it](mailto:scapasso@unisa.it) (S. Capasso).

<https://doi.org/10.1016/j.apenergy.2024.124508>

Received 29 February 2024; Received in revised form 20 August 2024; Accepted 12 September 2024

Available online 26 September 2024

0306-2619/© 2024 The Authors. Published by Elsevier Ltd. This is an open access article under the CC BY license (<http://creativecommons.org/licenses/by/4.0/>).

hydrodynamics that may result in different perceived wave characteristics, or wrong evaluations of orbital velocities, energy transport and, therefore, actions on structures. Currents nature and intensity varies around the globe: ocean current velocities have mean values around 0.2–0.6 m/s, and peaks above 2.5 m/s. Currents along the American North Atlantic coast, for example, have maximum speed of over 2.7 m/s, whereas Portugal current features maximum speed of 0.5 m/s [18]. Even higher velocities can be reached during tidal cycles in coastal areas, with main wave parameters heavily affected [19]; this holds true also for larger tidal phenomena, as in the Strait of Gibraltar, where the Atlantic jet pushes currents to speed above 1 m/s [20]. Their temporal variation scale stands at one order of magnitude further from the significant wave period, making it a steady component of the wave–current interaction problem. Including currents in spectral wave models may improve large-scale predictions and measurements, as it has been shown in [21].

Locally confined current influences on wave properties and their modification in terms of significant spectral components have been largely investigated. Most of the theoretical background was laid down during the '70s, and further refined in the early '90s with different approaches based on several working hypotheses, e.g., irrotational assumptions and steady currents. For what concerns the influence of the current on wave kinematics (wavelength, period) or dynamics (amplitude, energy conservation), and resulting orbital velocities, potential flow-derived solutions complying with different wave theories and current profiles are available [22]. Dean and Dalrymple [23] solved the interaction for airy waves and uniform currents; solutions for uniform currents and high-order waves are to be found, among others, in [24–27] and, including considerations on shoaling and variable depth bathymetry, in [28,29]. Results for linear and non-linear waves propagating over depth-varying currents are given in [30,31], respectively, adopting stream theory. Additionally, spectral properties modification in similar conditions have been investigated by Huang et al. [32].

Lately, the research attention has shifted towards more realistic characterizations of ocean environments including current effects, to address the need for accurate behavior assessment for ocean renewable energy devices [33]. Even when evaluating a system's response with simplified spectral models, in fact, the significant output parameters (among others, generated power, anchoring tension, wave loads) depend on the estimated wavelength, which is influenced by the potential presence of underlying currents by means of the Doppler shift. On the other hand, the representative frequency spectrum at a certain location may be strongly modified when following (with the same direction of wave propagation) or opposing (vice-versa) currents are considered [34], eventually affecting significant wave heights, steepness, and available wave power. As a result of this interest, a number of recent publications feature modified wave fields and/or frequency spectra in order to account for wave–current combination and relative action on marine structures. The work of Hashemi et al. [35] or Shi et al. [36], for example, analyzed the wave–current climate using an improved propagation model to obtain realistic estimate of power output from WEC devices in coastal zones which feature mighty tidal currents (peaks over 2 m/s). The results have shown a clear influence of currents firstly on the representative spectra, and eventually on the power production. These investigations show changes in the average absorbed power expected associated with joint distribution diagrams of significant wave height and period, sourcing the corresponding power value from each WEC power matrix.

Given the relevance of resource assessment and the accuracy of the developed wave–current evolution models, more refined hydrodynamics considerations may yield different WEC performance evaluations. In most of the cases, in fact, WECs power transfer functions are obtained without considering what can be defined as real thrust imposed by underlying currents and the resulting velocity field. For highly dynamic or relatively-light offshore structures, like point-absorber WECs [37],

semi-submersible [38], or spar-type FOWTs [39], a persistent and considerable shift in mean surge position induced by currents is very likely to occur. This causes undesired and, as such, neglected effects if the model disregards the non-zero volume flux. As a result of current-related loads, very compliant structures will seek new equilibrium positions, entailing novel unanticipated kinematics. It appears clear that the next necessary step to correctly include enlarged environmental actions within design stages, is represented by a deeper understanding of wave–current–structure interaction, as the different hydrodynamics is expected to invalidate the power matrix generated in pure wave conditions.

Numerical wave tanks based on CFD provide high levels of fidelity in conducting investigations for non-resolved waves and current interaction. However, they are yet to be applied for ORE. The authors are not aware of published investigations on waves and current derived hydrodynamics for WECs, whereas a few examples for FOWTs have employed low-fidelity models [38,39]. The advent of high-fidelity numerical testing for wave-moored structure interaction already impacted their development strategy [40], as CFD models can accurately estimate the interactions between WECs, and regular, irregular, or focused waves [41–47]. Likewise outcomes could be expected when enlarged environmental actions are included in advanced numerical solvers.

Most of the available tanks, however, are developed to investigate the non-linear combination of waves and current and thus arranged in two-dimensional fashion, and with longitudinal dimensions of several wavelengths, making the potential transition to realistic three-dimensional domains computationally unfeasible. Such layouts in mesh-based CFD solvers are used, for example, in Kumar and Hayatdavoodi [48] to investigate shallow water propagation of waves and current using open boundaries and relaxation zones (RZs), or to mimic experimental setups (see [49]) within a numerical framework [50] for similar purposes. Furthermore, inherent complications arise when moving objects are included in grid-based numerical domains; without ad-hoc techniques, mesh distortion could easily jeopardize their outcomes. The comprehensive review available in Oliveira et al. [51], in fact, shows that most of the developed mesh-based wave tanks, although reliable and precise, are mostly optimized for fixed wave–structure interaction, also when including current actions [52,53].

If, instead, the simulation of consistent displacements of floating objects and complex flow fields is targeted as such, the Lagrangian Smoothed Particles Hydrodynamics (SPH) method is certainly a viable option [54], coming without any need for special treatment of interfaces or re-meshing procedures [55]. As reviewed, a few SPH-based wave–current flumes are available in literature: in He et al. [56], the classic paddle-generated wave encounters an inflow pipe to recreate a current, whereas an outflow pipe is placed before a sponge layer, just as in experimental facilities; Ni et al. [57], instead, developed a tank based on open boundaries conditions, imposing depth-averaged signals at the inlet to recreate the required horizontal velocity field; similarly, open boundaries and a modified damping zone are implemented to recreate regular, irregular and focused waves over linearly sheared currents in [58]. The same authors, eventually, performed what can be possibly considered the first wave–current–structure interaction simulation within an SPH-based tank, successfully simulating extreme and breaking waves impacting a fixed monopile [59]. Table 1 summarizes the state-of-the-art numerical wave–current tanks, clearly highlighting the need for frameworks capable of simulating moving devices.

The open-source software DualSPHysics [61], which is based on the SPH method, offers a suitable computational framing within which we can develop a tank with the desired characteristics. DualSPHysics stands out for many relevant features for offshore renewable energy simulations, supporting most of recent numerical investigations regarding both WECs [42,43,62,63] and FOWTs [64–67]. This model is highly parallelized and optimized for Graphic Processing Units (GPUs) execution [68]. Couplings with external libraries makes it a valuable toolbox for supporting the design of multi-featured structures

**Table 1**  
CFD-based numerical wave flumes featuring waves and currents combined flows.

Reference	Software	Model	Wave generation	Wave absorption	Dimension	WSI
Zhang et al. (2018) [60]	In-house	RANS-VOF	Internal wavemaker + current inflow	Sponge layer + pressure outlet	2-D	None
Kim et al. (2016) [52]	FLUENT	RANS-VOF	Numerical wavemaker	Numerical beach	3-D	Fixed
Silva et al. (2016) [50]	ANSYS-CFX	RANS-VOF	Numerical wavemaker + inlet current flow	Numerical beach + outlet current flow	2-D	None
Li et al. (2018) [53]	OpenFOAM	RANS-VOF + FNPQ QALE-FEM	RZ coupling	n.a.	n.a.	Fixed
Kumar and Hayatdavoodi (2023) [48]	OpenFOAM	RANS-VOF	Numerical wavemaker + inlet current flow	Sponge layer + pressure outlet	2-D	None
He et al. (2018) [56]	In-house	SPH	Numerical wavemaker + inlet current flow	Sponge layer + outlet current flow	2-D	None
Ni et al. (2020) [57]	In-house	SPH	Imposed wave-current field at inlet	Damping zone + imposed outlet velocities	2-D	None
Yang et al. (2023) [58]	DualSPHysics	SPH	Imposed wave-current field at inlet	Damping zone + imposed outlet velocities	2-D	None
Yang et al. (2023) [59]	DualSPHysics	SPH	Imposed wave-current field at inlet	Damping zone + imposed outlet velocities	3-D	Fixed

RANS: Reynolds-averaged Navier–Stokes; VOF: Volume of Fluid; QALE-FEM: Quasi Arbitrary Lagrangian–Eulerian Finite Element Method; RZ: relaxation zone; In-house: code developed privately by the authors; n.a.: not attributable.

for energy harvesting, regardless of the toughness of the environmental scenario. Mechanical features, relevant for modeling PTOs, as well as multibody dynamics, contacts and kinematic restrictions are handled by the core Chrono module [69] via the two-way coupling interface developed in [70]. On the other hand, a revisited version of the mooring line model MoorDyn [71], known as MoorDynPlus, is coupled to DualSPHysics to provide catenary and taut-line anchoring models for floating objects [72]. The DualSPHysics framework encloses these additional features within a unified SPH-based environment with proven capabilities in simulating fluid-driven objects in harsh marine conditions [42], also with complex geometries [73].

Hence, within the DualSPHysics framework, a numerical multipurpose wave tank, complying with the necessary features for highly-dynamic structure testing, is implemented, validated, and applied to a point-absorber WEC to investigate its response when dealing with realistic oceanic conditions. This aims to unveil the distinct dynamics arising in complex marine structures, with several inherent sources of non-linearity, as PTO units or the taut-to-slack process in anchoring systems, when enduring coupled hydrodynamic loads generated by waves and currents in combination. To the authors' knowledge, this work represents the first detailed investigation into WEC dynamics with environmental loads as such, and the first attempt to evaluate the influence of similar combinations of factors onto the power yield of such devices.

Leveraging open boundaries [74] with improved boundary conditions interface [75], and a properly tuned relaxation zone [76] for wave absorption, the interaction of floating moored structures and high-order waves propagating over uniform currents is analyzed. An experimental campaign supporting the consequent numerical investigation is performed on a spherical buoy in tension-leg configuration, closely representing the taut-line point-absorber eventually scrutinized, embodied by the Uppsala University WEC (UUWEC) [77]. Complete validation in DualSPHysics for this device was presented in [42], according to an experimental campaign proposed in [78]. The proposed results show that clear influence of the underlying current arises when considering the device dynamics and its power production. Prospective research and development of WECs should aim to include these modifications when site-specific conditions, or even general guidelines [79], envision a possible coexistence of waves and current. Apt for moored structures and coming with sustainable computational effort, the wave-current flume can install various types of complex moving structures without any particular adaptation strategy, providing researchers and designers alike with a powerful high-fidelity tool with a broad range

of mechanical, structural, and environmental simulation capabilities, relying on the known SPH performance in handling WSI [80].

The manuscript is organized as follows: firstly, the numerical framework of DualSPHysics is presented in Section 2, with details on the SPH method and the available couplings utilized; numerical flume development for the purposes of this research is detailed in Section 3, including a validation for wave propagation and wave–structure interaction against experimental data. Section 4 describes the numerical campaign on the UUWEC and outlines the insights obtained on the validated model; finally, conclusions and future research prospects are gathered in Section 5.

## 2. Numerical model

The fully Lagrangian Smoothed Particle Hydrodynamics method is based on the discretization of the physical domain in nodal points, namely particles, carrying individual properties and operating as moving computational nodes. In each of these nodes, relevant physical quantities are obtained through interpolation from the corresponding quantities of the surrounding particles [55]. This numerical scheme is ruled by a weighting function via the characteristic smoothing length, defining the number of neighboring particles interacting with each node and pondering the interaction on the relative distance between particles [81].

### 2.1. SPH discretization

Numerical models based on the SPH method rely on two consequential approximations to represent integrable functions, performed at continuous and discrete levels, respectively. Firstly, spatial functions  $f(\mathbf{r})$  are represented, within their integral volume  $\Omega$ , by their kernel approximation:

$$\langle f(\mathbf{r}) \rangle = \int_{\Omega} f(\mathbf{r}') W(\mathbf{r} - \mathbf{r}', h) d\mathbf{r}'. \quad (1)$$

In other words, the value of  $f$  in a generic position  $\mathbf{r}$  can be approximated by integrating the values of the function in other points belonging to the same domain,  $\mathbf{r}'$ , multiplied by the kernel function  $W$ , namely a continuous representation of the Dirac delta function. The smoothing kernel's area of influence is defined by the smoothing length  $h$ ; if  $h \rightarrow 0$ , the integral representation would be exact.

The ensuing step allows for the evaluation of the integral in Eq. (1) within a discrete defined space. The so-called particle approximation yields:

$$\langle f(\mathbf{r}) \rangle = \sum_{b \in S_N} \Delta V_b f(\mathbf{r}_b) W(\mathbf{r} - \mathbf{r}_b, h), \quad (2)$$

representing the summation of the values of  $f$  over all particles  $b$  belonging to the support  $S_N$ , multiplied by the kernel function and their own volume  $\Delta V_b$  [82]. The kernel function is expected to fulfill several properties, such as positivity, smoothness, decay, or compactness [83]. In this work, the complying polynomial Quintic Wendland kernel [84] has been utilized with the smoothing length set to  $2h$ .

## 2.2. Weakly compressible formulation

In fluid dynamics, the Navier–Stokes equations describe the flow motion. For compressible fluids and in Lagrangian form, the system reads:

$$\frac{d\mathbf{u}}{dt} = -\frac{1}{\rho} \nabla p + \mathbf{g} + \mathbf{I}, \quad (3)$$

$$\frac{d\rho}{dt} = -\rho \nabla \cdot \mathbf{u}, \quad (4)$$

with  $\rho$  being particle density,  $\mathbf{u}$  the velocity vector,  $\mathbf{g}$  the gravitational acceleration vector, and  $p$  the pressure;  $\mathbf{I}$  denotes a dissipation term. When explicit SPH implementation is applied to compressible fluids, as in DualSPHysics, a supplementary equation of state is needed to relate changes in density and fluid pressure:

$$p = \frac{c_s^2 \rho_0}{\gamma} \left( \left( \frac{\rho}{\rho_0} \right)^\gamma - 1 \right), \quad (5)$$

where  $\rho_0 = 1000 \text{ kg/m}^3$  is the reference fluid density,  $\gamma = 7$  is the polytropic constant,  $c_s$  is the numerical speed of sound. Expected density variations of less than 1% make the results of this approach comparable to incompressible SPH formulations. Reflecting such small fluctuations, this approach is usually referred to as Weakly Compressible SPH (WCSPH). Coming at the cost of very small time steps, this scheme is indeed suitable for massive parallel computing [68].

Let  $a$  be the extant computational point, and  $b$  one of the  $N_p$  particles included in the neighboring set  $S_N$ . The WCSPH discretization of the Navier–Stokes equations reads:

$$\frac{d\mathbf{u}_a}{dt} = -\sum_{b=1}^{N_p} m_b \left( \frac{p_b + p_a}{\rho_a \rho_b} + \Pi_{ab} \right) \cdot \nabla_a W_{ab} + \mathbf{g}, \quad (6)$$

$$\frac{d\rho_a}{dt} = \sum_{b=1}^{N_p} m_b \mathbf{u}_{ab} \cdot \nabla_a W_{ab} + D_a, \quad (7)$$

with  $\mathbf{u}_{ab} = \mathbf{u}_a - \mathbf{u}_b$ . In the momentum equation (6), an artificial viscosity term,  $\Pi_{ab}$ , is added in the momentum equation based on the Neumann–Richtmeyer artificial viscosity, aiming at stabilizing the SPH scheme [83]. It dissipates high frequency modes with an intensity depending on relative particles velocity and positions, and a parameter  $\alpha$ , usually set equal to 0.01:

$$\Pi_{ab} = \begin{cases} \frac{-\alpha \bar{c}_{s,ab} \mu_{ab}}{\bar{\rho}_{ab}} & \mathbf{u}_{ab} \cdot \mathbf{r}_{ab} < 0 \\ 0 & \mathbf{u}_{ab} \cdot \mathbf{r}_{ab} > 0, \end{cases} \quad (8)$$

where  $\mathbf{r}_{ab} = \mathbf{r}_a - \mathbf{r}_b$  and

$$\begin{aligned} \mu_{ab} &= \frac{h \mathbf{u}_{ab} \cdot \mathbf{r}_{ab}}{|\mathbf{r}_{ab}|^2 + \eta^2}, \\ \bar{c}_{s,ab} &= \frac{1}{2}(c_{s,a} + c_{s,b}), \\ \bar{\rho}_{ab} &= \frac{1}{2}(\rho_a + \rho_b), \\ \eta^2 &= 0.001 h^2. \end{aligned}$$

The continuity equation Eq. (7), instead, features a density diffusion term to reduce density fluctuations, following Fourtakas et al. [85], that is expressed as:

$$D_a = 2\delta h c_s \sum_b (\rho_{ab}^T - \rho_{ab}^H) \frac{\mathbf{r}_{ab} \cdot \nabla_a W_{ab}}{r_{ab}^2} \frac{m_b}{\rho_b}, \quad (9)$$

where  $\delta = 0.10$  is the coefficient that controls the diffusive process, and superscripts  $T$  and  $H$  identify the total and hydrostatic components of the density, respectively, that characterize weakly compressible fluids.

This term is implemented to improve the stability of the scheme by smoothing the density field. Based on the formulation proposed by Molteni and Colagrossi [86], which, however, leads to some inconsistencies near the wall boundaries, it was further improved as detailed in [85]. The total dynamic density is replaced with the dynamic density so the pressure close to wall boundaries becomes consistent with the pattern exhibited by the surrounding fluid particles. As opposed to the delta-SPH formulation proposed by Antuono et al. [87], which is certainly applicable in various physical cases, this approach eliminates the need for computing the normalized density gradient, saving computational cost. Nevertheless, for gravity-dominated flows the proposed approach delivers reliable results [85]. The presented set of equations is solved using a second-order accurate Symplectic time integrator [88] with a variable time stepping satisfying Courant–Friedrichs–Lewy (CFL), viscous diffusion and force term-dependent conditions. More details in [61].

### 2.2.1. Rigid body dynamics and SPH

The motion of objects interacting with fluids is handled by Newton's equations for rigid body dynamics, with the force contribution being computed among the surrounding fluid particles. According to the designated kernel and smoothing length, the net force on each boundary particle  $k$  is computed as:

$$\mathbf{f}_k = \mathbf{g} + \sum_{b \in S_{N,f}} \mathbf{f}_{kb}, \quad (10)$$

where  $\mathbf{f}_{kb}$  is the force per unit mass exerted by the fluid particle  $b$ , included in the neighboring fluid set  $S_{N,f}$ , on the boundary particle  $k$ . In the SPH approximation, with  $S_{N,b}$  gathering body's particles, the Newton's equations read:

$$M \frac{d\mathbf{V}}{dt} = \sum_{k \in S_{N,b}} m_k \mathbf{f}_k, \quad (11)$$

$$\mathbf{I} \frac{d\boldsymbol{\Omega}}{dt} = \sum_{k \in S_{N,b}} m_k (\mathbf{r}_k - \mathbf{r}_0) \times \mathbf{f}_k, \quad (12)$$

where  $M$  is the mass,  $\mathbf{I}$  the inertia matrix,  $\mathbf{V}$  the velocity,  $\boldsymbol{\Omega}$  the angular velocity, and  $\mathbf{r}_0$  the center of mass position;  $\times$  indicates the cross product. Each boundary particle within the body has a velocity given by:

$$\mathbf{u}_k = \mathbf{V} + \boldsymbol{\Omega} \times (\mathbf{r}_k - \mathbf{r}_0). \quad (13)$$

The integration in time of Eqs. (11) and (12) returns the actual motion of the object, computing velocities with Eq. (13). The work by Monaghan et al. [89] showed that linear and angular momentum are conservative properties; further validations about buoyancy-driven motion are performed in [72,90].

### 2.3. Boundary conditions

This section presents the general solid boundary treatment and the open boundary scheme adopted throughout the investigation.

### 2.3.1. Solid boundaries

The modified Dynamic Boundary Conditions (mDBC) [91] are the standard solid boundary conditions adopted in this study. As an evolution of the Dynamic Boundary Conditions (DBC) [92], effectively and largely adopted for complex geometries [93], mDBC improves the performance of the former approach, especially when not-wet boundary particles eventually interact with fluid. Using the same particle arrangement of DBC, an interacting boundary surface is added between the outermost layer of particles of the body and the fluid domain. Normal vectors are computed with respect to the latter boundary surface for all the particles within a certain distance, usually equal or slightly greater than the smoothing length. This means that a certain number of layers of boundary particles has to be placed within the boundary element depending on the smoothing length. The interface location, hence, is used to mirror ghost nodes into the fluid domain, where a first-order consistent SPH spatial interpolation only provides the field properties [94] over the surrounding particles. Eventually, these properties are used to extrapolate the density values of the boundary particles, homogenizing the boundary and fluid pressure fields and solving the over dissipation of the former approach. Using DBC, in fact, non-physical forces developed at the interface as a consequence of the repulsive force created by the increasing density of the approaching fluid particle. This often resulted in large gaps between the boundary and the first fluid particles layer, and spurious pressure field [95], which is avoided with the mDBC approach. Applications for various kinds of FSI can be found in [73,96–99].

### 2.3.2. Open boundaries

The chosen open boundary algorithm has been implemented in DualSPHysics by Tafuni et al. [74], using a ghost node mirroring technique deduced from the closed boundary treatment of Marrone et al. [100]. Inlet/outlet buffer particles, arranged in several layers, are placed beyond the domain edge, namely the buffer threshold, with properties either imposed or extrapolated from the fluid. Particle quantities are obtained at ghost nodes using a corrected kernel gradient [81] to counter the lack of kernel support completeness. With this approach, the buffer can operate as an inlet or outlet depending on the problem to be simulated; when buffer particles cross the buffer threshold, they are included in the physical domain as fluid particles, and vice versa at the outlet. Open boundaries have been extensively validated for wave propagation in [101] or for two-way coupling with propagation models [102]: particles velocity and free surface elevation derived from wave theories or other solvers can be imposed at inlet/outlet. Verbrugge et al. [101] shows that eight layers of buffer particles are enough to provide optimal wave propagation. With the latest improvements for flow definition presented in [75], the open boundary can now enforce a two-dimensional grid with the required spatial and temporal resolution, guaranteeing efficient control on the SPH particles velocities at the inlet boundary. In this work, open boundaries provide the necessary flexibility to simulate wave–current–structure interaction problems, as shown in similar contexts [103,104].

### 2.4. Mechanical features

To extend the capability of the SPH-based framework of DualSPHysics to act as a multiphysics solver, a two-way coupling with the Chrono library [69] has been firstly proposed in [105] and further extended by Martínez-Estévez et al. [70], in which a general purpose interface, DSPHChronoLib, has been implemented. This library manages data conversion and synchronization, unleashing the capabilities of the Chrono core module: it supports large multibody simulations, applies kinematic and dynamics restrictions, and solves smooth and non-smooth contacts. In this work, the coupling is utilized to simulate the mechanical features of the UUWEC, with a linear PTO modeled as per [42], which includes contact mechanics and mechanical restrictions.

Solid objects are discretized as a set of particles and behave according to Eqs. (11) and (12); when the distance ( $\delta_{xy}$ ) between different solids is within the interaction radius (overlap distance  $\delta_n$ ), the soft-body discrete element method (DEM) implemented in the Chrono module solves the contact mechanics. It is known as DEM-P because it is based on a penalty methodology that allows penetration between bodies to obtain a partial deformation from the contact [69], and it is solved via differential algebraic equations (DAE). When two collision shapes, namely the corresponding Chrono objects for solid SPH bodies, partially overlap ( $\delta_{xy} < \delta_n$ ), normal and tangential forces are computed according to the Hertzian theory [106]. For linear PTOs, tangential forces are negligible due to the imposed linear vertical motion of the generator. The ruling normal contact force is, hence:

$$\mathbf{F}_n = \sqrt{R\delta_n}(k_n \mathbf{x}_n - c_n \bar{m} \mathbf{u}_n^*), \quad (14)$$

where  $\mathbf{x}_n$  is the local normal deformation,  $\mathbf{u}_n^*$  the normal component of relative velocity at contact point,  $k_n$  and  $c_n$  the normal stiffness and damping coefficients depending on the material properties,  $\bar{R}$  and  $\bar{m}$  the effective radius of curvature and mass, respectively. If two bodies  $x$  and  $y$ , of mass  $m_x$  and  $m_y$ , and contact radii of curvature  $R_x$  and  $R_y$  collide, then  $\bar{m} = m_x m_y / (m_x + m_y)$  and  $\bar{R} = R_x R_y / (R_x + R_y)$ . With this additional forcing condition, communicated to DualSPHysics through DSPHChronoLib, Eqs. (11) and (12) update particle velocity and position.

Mechanical restrictions, on the other hand, are provided via additional forcing terms on the set of rigid bodies. To represent the PTO mechanism, a spring–damper–actuator formulation is used, providing an additional force along the PTO axis,  $z$ :

$$F_c = k_c(d_c - l_s) + c_c u_z \quad (15)$$

with  $d_c$  being the distance between the bodies,  $l_s$  the equilibrium length of the spring,  $u_z$  the axial component of velocity experienced by the constraint. The term  $k_c$  represents the spring stiffness, and  $c_c$  the damping. Extended treatment of the ruling equations and coupling strategy is provided in [70].

### 2.5. Mooring line solver

The lumped-mass mooring line model MoorDynPlus [107], coupled with DualSPHysics following the methodology presented in Domínguez et al. [72], provides the dynamics of the moorings of floating objects or structures. It is able to account for axial stiffness, damping, weight and buoyancy forces, and also vertical spring–damper forces due to the possible friction with seabed. Hydrodynamic forces, instead, are calculated from Morison’s equation under the assumption of quiescent water. It follows that the mooring line itself does not account for the physical interaction with waves and currents; in the particular cases eventually displayed, nevertheless, the limited mass and footprint of the anchoring systems comply with this simplifying hypothesis.

MoorDynPlus boasts several features, such as interconnected floating bodies or different depths for catenary-like connections. The library resolves the mooring structural dynamics (only reacting to tension forces) by means of a lumped-mass discretization. If the mooring has an unstretched length  $l_{0,M}$ ,  $N_M + 1$  nodes are separated by  $N_M$  segments of length  $l = l_{0,M} / N_M$ . At each SPH time step, information about position and velocity of the moored body are passed to MoorDynPlus, which calculates, in one or more iterations, the tension at the anchor and fairlead points. The latter tension values are passed back to let DualSPHysics solve Eqs. (11) and (12), and integrate the object motion in time through Eq. (13). Further information on the coupling is available in [72].

### 3. Multipurpose wave flume

In this section, the implementation and validation of the multipurpose numerical wave flume is presented. Relying on the divergence-free solution of the combination of third-order Stokes' waves and uniform current, flow velocity field and free-surface evolution are computed. Such information is then enforced within the SPH-based flume using open boundaries and tuned passive absorption. Wave-current propagation and wave-current-structure interaction are validated against experimental data, proving the reliability of the numerical environment, thereby utilized for the numerical investigation carried out in Section 4.

#### 3.1. Considerations on wave-current theories for load definition purposes

Some words need to be spent in order to clarify the different approaches available in literature and, hence, the different expected outcomes. The core modifications experienced by a wave traveling over a following current in intermediate or deep water conditions can be resumed by the wave profile stretching, featuring sensitive increases of wavelength and reduction of wave height – i.e., decreased steepness; an opposed behavior is observed with opposing currents – i.e., increased steepness. Formulae for the solution of the modified wave profile can be found in [23,25,108], grounding on a well-posed system of equations to obtain the current-modified parameters (i.e., wave height,  $H$ , wavenumber,  $\kappa$ , and angular frequency,  $\omega$ ) starting from their wave-only counterparts in absence of current ( $H_0$ ,  $\kappa_0$ ,  $\omega_0$ ). Such a method is usually applied in combined wave-current prediction models to assess the variation of the wave properties according to tidal cycles or periodic changes of wind-generated or oceanic currents. The outcomes, in most cases, are conducive to estimating ocean power resources [35,109] and eventually WEC performance [36] in location where field measurements are available on every parameter, including the time-varying current value, and implemented in properly modified wave propagation models [110,111].

On the other hand, local solutions of the wave-current interaction can be formulated with  $H$ ,  $\omega$  as prior data, and considering an unknown wavenumber  $\kappa = 2\pi/\lambda$ ,  $\lambda$  being the wavelength [24,25]. This is a convenient approach when current measurements are not available or unreliable, and the flow field has to be solved to comply with measured values of wave height and period.

These different procedures can lead to likewise conclusions, especially regarding the mean available power associated with a determined wave-current condition. In spectral representation,  $f$  being the frequency, let:

$$J = \int \rho g S(f) c_g(f) df, \quad (16)$$

be the total energy flux in a wave spectrum  $S(f)$ , with

$$c_g = \frac{\omega}{2\kappa} \left( 1 + \frac{2\kappa d}{\sinh(2\kappa d)} \right) \quad (17)$$

representing the group velocity. As the spectrum can either include or not changes in wave height and wavenumber, it may provide wrong estimates of the available wave power. Formulae for computing current-modified spectra are given in [34], along with a careful discussion of the application of such approach by [109] (using  $H$  and  $\kappa_0$ ) and [35] (using  $H$  and  $\kappa$ ): increase in wave height appear to influence the wave power as opposing currents result in an *inflation* of the energy density, but the magnitude of this change is mitigated if the correct wavelength estimation is included, i.e., rightfully adopting  $\kappa$  instead of  $\kappa_0$ .

The use of local solutions, instead, without modifying the wave amplitude, yields increased available power as the following current value increases:

$$J = \rho g \frac{H^2}{8} c_g, \quad (18)$$

being  $c_g$  dependent on the wavenumber (see Fig. 20 in Appendix A).

**Table 2**  
Nomenclature used in Section 3.2.

$a_i$	$m$ -th order wave amplitude
$H$	Wave height
$\lambda$	Wavelength
$\kappa = 2\pi/\lambda$	Wavenumber
$\varepsilon = \kappa H/2$	Wave steepness
$T$	Wave period
$\omega = 2\pi/T$	Angular frequency
$d$	Water depth
$U_0$	Mean horizontal velocity in the AFR
$\bar{U}$	Mean horizontal velocity in the RFR
$c$	Phase velocity
$c_g$	Group velocity
$Q$	Volume flow rate per unit width
$U_2$	Mean fluid transport velocity

The purpose of this research is to provide a high-fidelity tool for evaluating the actual wave-current-structure interaction, rather than analyzing the availability or evolution of wave power and its dependence on the current features. To fulfill this aim, the most appropriate strategy, also considering the implementation of the wave-current field in a compact numerical tank, is to use the single unknown approaches as per [24,25], considering the wave height as datum. Doing so, the developed wave flume will ultimately be able to relate, using a transfer function, the performance of the wave energy converter to arbitrary points in the environmental space defined by wave parameters and current features, with possible straightforward applications to any kind of floating offshore energy device. Afterwards, considerations on the local modification of the frequency spectrum can be looked into, as any sea-state realization can be represented, under some assumptions, as a combination of values from the proposed physical-based transfer function.

#### 3.2. Waves over steady uniform current

The interaction between pure high-order waves and uniform currents (normal to the wave crest) yields to the definition of combined wave-current velocity fields by assuming flat-bed, neglecting dissipation (fluid inviscid and incompressible), and considering irrotational collinear currents. The following governing equations (velocity potential, free-surface elevation, particle velocities) are written according to the results obtained in [25], using the wave speed and dispersion relation as proposed in [24]. For the sake of clarity, the nomenclature is reported in Table 2. Hence, the solution is obtained by considering  $H$ ,  $T$ ,  $d$  and  $U_0$  as known data, with  $\lambda$  as the only unknown of the problem [112].

The most intuitive approach to tackle wave-current interactions as such is to use two frames of reference, one absolute (AFR), with respect to which the problem solution has to be expressed, and one, relative (RFR), traveling along with the wave crest with velocity  $c$ . The Eulerian mean velocity measured by a fixed observer (AFR) would be  $U_0$ , whereas, the mean horizontal velocity in the RFR would be  $-\bar{U}$  (relative phase velocity). The term  $U_0$  is sometimes referred to as “mean current-like term”, as it represents with good approximation a constant value of current traveling together with the waves. With this meaning,  $U_0$  is adopted in this work to indicate the uniform current velocity, as in [23,24], for example. Most theories provide ways to retrieve  $\bar{U}$ : with information on  $U_0$  and using Stokes' first approximation to wave speed,

$$U_0 = c - \bar{U}, \quad (19)$$

it is possible to obtain the solution rather simply. The dispersion relation provided by Stokes, retaining terms up to the second order, is valid for third-order accurate flow description [26]:

$$\bar{U} \sqrt{\frac{\kappa}{g}} = C_0(\kappa, d) + \varepsilon^2 C_2(\kappa, d) + \mathcal{O}(\varepsilon^4) \quad (20)$$

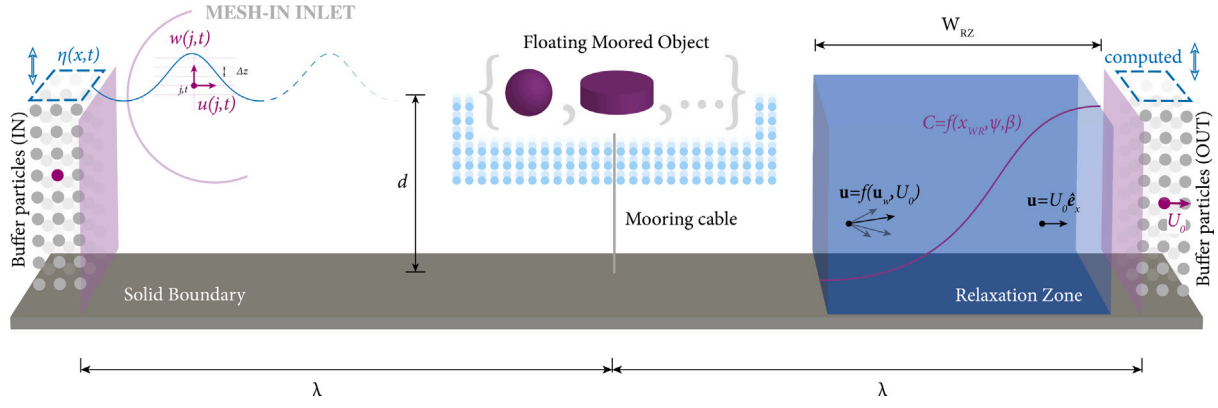


Fig. 1. Numerical wave-current flume as implemented in DualSPHysics, with details of the inlet-outlet zones.

where

$$\begin{aligned} C_0 &= \sqrt{\tanh(\kappa d)}, \\ C_2 &= C_0(2 + 7S^2)/(4(1 - S^2)), \\ S &= \operatorname{sech}(2\kappa d), \end{aligned}$$

and  $\mathcal{O}(\cdot)$  is the Landau order symbol representing the neglected terms. Substituting Eq. (19) in Eq. (20) and rearranging the terms in  $\kappa$  gives:

$$\sqrt{\frac{\kappa}{g}}U_0 - \frac{2\pi}{T\sqrt{g\kappa}} + C_0 + \varepsilon^2 C_2 + \mathcal{O}(\varepsilon^4) = 0. \quad (21)$$

This nonlinear transcendental equation usually, that is, the dispersion relation, can be solved numerically to obtain the wavenumber. A similar expression would be available if the volume flow  $Q$  were known instead of  $U_0$ , relying on Stokes' second approximation to wave speed:

$$U_2 = c - Q/d. \quad (22)$$

Once the problem is completely defined, i.e., the wavelength has been determined with Eq. (21), it is possible to obtain the flow characteristics applying Stokes theory [25]. According to the problem hypotheses, a velocity potential function  $\Phi(x, z, t)$  that satisfies Laplace's equation can be defined. Let  $O\{x, z\}$  be the fixed reference system, placed on the undisturbed free-surface with the vertical axis pointing upwards. Three boundary conditions need to be defined for the periodic problem in  $x$  and  $t$ : (i) impermeable horizontal bottom boundary condition, (ii) kinematic free-surface, and (iii) dynamic free-surface boundary condition. They read:

$$\begin{aligned} \Phi_z &= 0 && \text{on } z = -d, && (i) \\ \Phi_z &= \eta_t + \Phi_x \eta_x && \text{on } z = \eta(x, t), && (ii) \\ R &= g\eta + \Phi_t + \frac{1}{2}(\Phi_x^2 + \Phi_z^2) && \text{on } z = \eta(x, t), && (iii) \end{aligned}$$

with the subscript denoting partial differentiation ( $(\cdot)_x := \partial(\cdot)/\partial x$ ) and  $R$  representing Bernoulli's constant — see Appendix A. The free-surface elevation function could be reasonably stated, considering the third-order solution, as

$$\eta(x, t) = \sum_{m=1}^3 a_m \cos m(\kappa x - \omega t). \quad (23)$$

Given the periodicity of  $\eta(x, t)$ ,  $\Phi(x, z, t)$  can be expressed as:

$$\Phi(x, z, t) = A_0(z)x + \sum_{n=1}^3 A_n(z) \sin n(\kappa x - \omega t), \quad (24)$$

with the coefficients  $A_{0,1,2,3}$  expressed as functions of  $z$  only. Imposing the compliance to the Laplace's equation, namely  $\nabla^2 \Phi(x, z, t) = 0$ , and applying the boundary conditions, the expressions for free-surface elevation and velocity potential can be deduced as functions of the parameters  $a_m$  and  $A_n$ , reported in Appendix A.

Horizontal and vertical particle velocities are obtained as spatial derivatives of the velocity potentials,  $u(x, z, t) = \Phi_{x,z}$ ,  $w(x, z, t) = \Phi_{z,z}$ , and expressed as:

$$\begin{aligned} u &= U_0 + \frac{a_1 \omega_R}{\sinh \kappa d} \cosh \kappa(z+d) \cos(\kappa x - \omega t) \\ &+ \frac{3}{4} a_1^2 \omega_R \kappa \frac{\sinh 2\kappa(z+d)}{\sinh \kappa d^4} \cos 2(\kappa x - \omega t) \\ &+ \frac{3}{64} a_1^3 \omega_R \kappa^2 \frac{11 - 2 \cosh 2\kappa d}{\sinh \kappa d^7} \cosh 3\kappa(z+d) \cos 2(\kappa x - \omega t), \\ w &= \frac{a_1 \omega_R}{\sinh \kappa d} \sinh \kappa(z+d) \sin(\kappa x - \omega t) \\ &+ \frac{3}{4} a_1^2 \omega_R \kappa \frac{\sinh 2\kappa(z+d)}{\sinh \kappa d^4} \sin 2(\kappa x - \omega t) \\ &+ \frac{3}{64} a_1^3 \omega_R \kappa^2 \frac{11 - 2 \cosh 2\kappa d}{\sinh \kappa d^7} \sinh 3\kappa(z+d) \sin 2(\kappa x - \omega t); \end{aligned} \quad (25)$$

where  $\omega_R$  is the relative angular frequency that satisfies the Doppler relation,

$$\omega = \omega_R + \kappa U_0. \quad (26)$$

### 3.3. Flume implementation

The three-dimensional wave flume developed to investigate wave-current-structure interaction is implemented in DualSPHysics leveraging multiple features from the code (Fig. 1). Its dimension is constrained, longitudinally, to two wavelengths, with open boundaries [74] placed on both sides to produce the desired flow condition. This choice ensures proper wave propagation of regular waves within the first wavelength, and absorption within the second. The transverse dimension is problem-dependent and it is designed to avoid lateral effects using periodic boundaries [113], or to mimic experimental flumes with solid boundaries. Fig. 1 details the computational domain: the numerical space is initialized with SPH particles representing both fluid and solid objects, gathered in different sets, and placed according to a regular lattice spaced at  $dp$ , which defines this model resolution. The structure with its own features provided by the coupled libraries (mooring connection – mechanical restrictions – PTO systems) may be placed in the middle of the tank.

#### 3.3.1. Meshed inlet for high order waves

At the inlet, particle velocities (Eq. (25)) and free-surface elevation (Eq. (23)) are obtained in pre-processing and enforced using a spatial grid interpolation method [75]. Particle density is, instead, extrapolated from the fluid domain. The grid resolution  $\Delta z$  corresponds to half the particle spacing  $dp$  and the external signal is imposed with a frequency of 1000 Hz, a value close to the average SPH time step size for the considered simulations. Since the flow properties do not vary along  $y$ , the same values of velocity are imposed on all the particles sharing the same  $z$  coordinate. With such implementation, it is possible

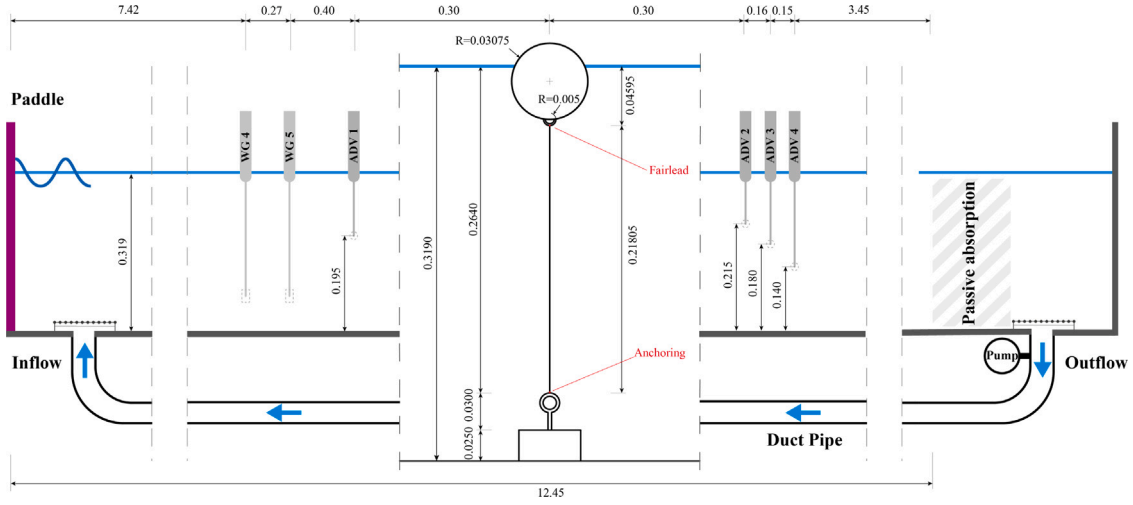


Fig. 2. Scheme of the experimental setup, reporting wave gauges and ADV placement; in detail the dimension of the spherical wave buoy.

to define particle velocities, which are described by high-order Stokes theories, up to the time-varying free-surface level, which is reproduced in DualSPHysics by adding and subtracting horizontal buffer particle layers.

For high steepness waves, this implementation sensibly improves the wave profile accuracy and reduces the propagation space in which the wave is completely developed. At the outlet zone (right-end side of Fig. 1), the velocity of the particles is set to be equal to the mean current speed  $U_0$ , whereas density and free-surface elevation are computed from the adjacent fluid particles.

### 3.3.2. Absorption layer

To comply with the outlet condition, the wave-dependent velocity components and the perturbation caused by the interaction with the moored structure need to be damped out. A modified relaxation zone (RZ) [114] of dimension  $W_{RZ}$  is placed between the structure and the outlet buffer layer to avoid wave reflection and ensure constant inflow/outflow balance. The RZ applies a progressive correction on particle velocity, depending on their relative position  $x_{WR}$ , according to a smoothing curve  $C(x_{WR}, \psi, \beta)$ . Coefficients  $\psi$  and  $\beta$  shape the function, and the parameter  $\bar{\gamma}$  modulates the intensity of the correction. At each time step  $\Delta t_{SPH}$ , the velocity component along the direction  $\hat{e}_i$  is updated as:

$$u_{\hat{e}} = C\bar{\gamma}\Delta t_{SPH}v_{\hat{e}} + (1 - C\bar{\gamma}\Delta t_{SPH})u_{\hat{e}}, \quad (27)$$

with  $v_{\hat{e}}$  being the corresponding target velocity component, i.e.  $U_0$  horizontally, and 0 in the other two directions.

A pre-processing tool based on the intended wave condition has been implemented to fully harness the RZ length, hence limiting wave reflection and guaranteeing the targeted velocity field. The dimension and shape of the curve being set by  $W_{RZ} = 0.8\lambda$ ,  $\psi = 0.8$ ,  $\beta = 3$ , the coefficient  $\bar{\gamma}$  is estimated depending on the calculated phase velocity, as per Eq. (19). Within this offline simplified routine, a wave traveling with celerity  $c$  is progressively damped using Eq. (27) and a penalizing term that mimics particles inertia. This allows to evaluate the correct  $\bar{\gamma}$  to achieve the mean current value at the very end of the RZ. In this way, the performance of the RZ is automatically optimized, speeding up the setting up process and lightening the computational effort by keeping the SPH domain dimension under an acceptable threshold.

## 3.4. Flume validation

To validate the proposed wave flume for both wave-current propagation and FSI, an experimental campaign has been conducted in the CIEMito wave flume of the CiemLab, at the Laboratori d'Enginyeria Marítima (LIM) of the Universitat Politècnica de Catalunya – BarcelonaTech, Spain.

### 3.4.1. Experimental setup

The CIEMito (Fig. 2) has an effective length (paddle-to-absorption layer) of 12.45 m, and is 0.38-m wide. This wave flume is equipped with a current generation system that recirculates water through a duct pipe placed under the canal; the inflow point of the pipe is placed right after the wave paddle and protected by a metallic rack to avoid excessive turbulence in the interaction region, whereas the outflow point lies after the passive absorption layer. Such relative position of passive absorption and current outflow pipe did not allow for long runs: an average of 4 waves per wave condition is herein considered. Data from resistive wave probes (with sampling frequency of 80 Hz) and Acoustic Doppler Velocimetry (ADV) (sampling frequency 20 Hz) are used to validate the wave-current conditions in the DualSPHysics simulations. Sensor placements and flume dimensions are detailed in Fig. 2. With such experimental configuration, the current profile has been measured to be acceptably uniform and steady if far from the pipe inflow, coherently with the theoretical approach described in Section 3.2 and with the observations of [49,115]. Further description of the flume and acquisition system is provided in [104]. The central panel of Fig. 2 shows the detailed dimensions of the moored spherical buoy with taut-line anchoring used for WSI validation purposes, which is further characterized in Section 3.4.3. Empty tank tests (without the buoy) and WSI tests (with the buoy) in various wave conditions and mean current speed have been performed three times each to ensure their repeatability.

Table 3 reports the sea states executed in the CIEMito as imposed at paddle and measured ( $\cdot$ )<sub>me</sub> at WG4 and WG5. The measured values are then used as input parameters for the DualSPHysics simulation for both wave propagation and WSI validation; for easiness of understanding, conditions C1, C2 and C3 are also identified throughout the validation phase with the imposed wave height, period, and mean current speed ( $H, T, U_0$ ). In Table 3, the Ursell number is also reported to ensure the reliability of the adopted wave theory when underlying currents are included [116]. As in all conditions the Ursell number is under the limit threshold of 40, the third order Stokes' solution is considered valid.

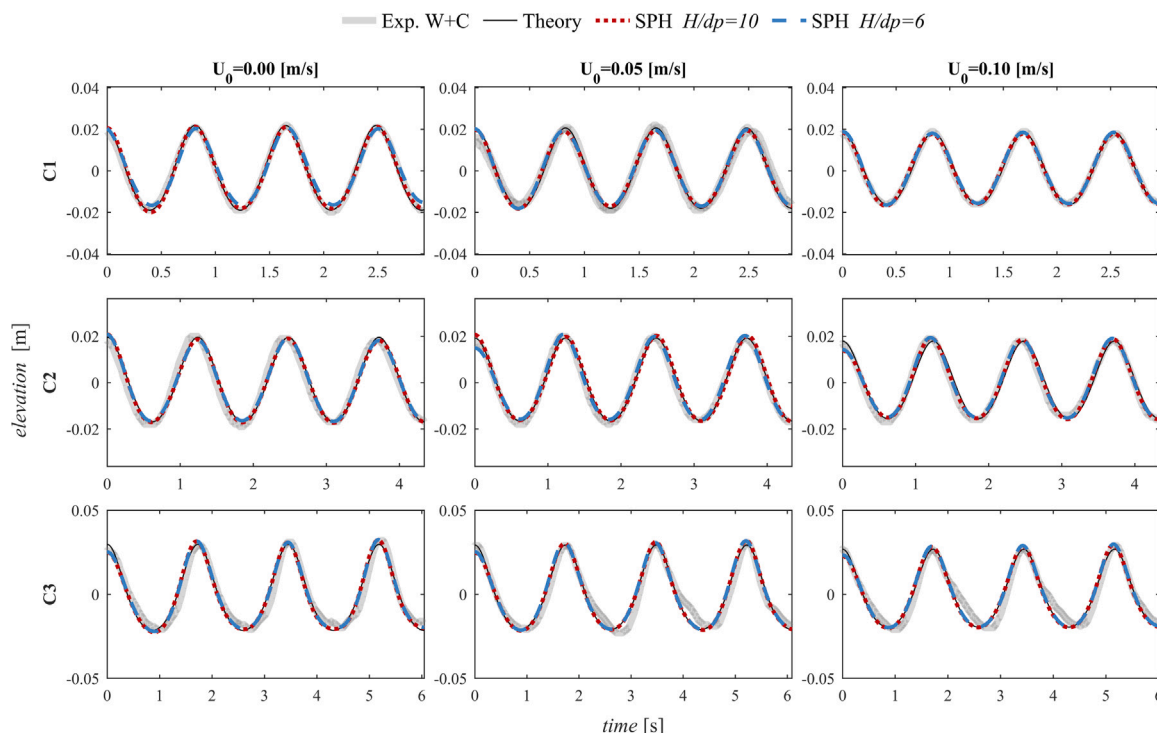
### 3.4.2. Wave-current validation

Fig. 3 depicts the empty-flume validation for the considered waves and current cases, whose input values are listed with subscript ( $\cdot$ )<sub>me</sub> in Table 3. Wave conditions and mean current velocities in Fig. 3 are ordered in rows and columns, respectively. The experimental measurements are averaged among the three repetitions and the two wave gauges WG4 and WG5, placed right before the moored sphere. The numerical simulations are performed in a 2-D domain, and two resolutions are used: six ( $H/dp = 6$ ) and ten particles ( $H/dp = 10$ ) from

**Table 3**

Wave conditions as measured in the experimental flume, for which depth is set to 0.319 m and kept constant for all the tests.

	Imposed		Stokes' theory	$U_0$	Measured – ( $\cdot$ ) <sub>me</sub>					
	$H$	$T$			$H_{me}$	$T_{me}$	$U_{0,me}$	$\lambda$	$\epsilon$	Ursell n.
<b>C1</b>	0.05	0.85	II	0.00	0.0405	0.8371	0.00	1.06	0.120	1.41
				0.05	0.0384	0.8273	0.05	1.11	0.110	1.45
				0.10	0.0346	0.8452	0.09	1.20	0.091	1.53
<b>C2</b>	0.05	1.25	II	0.00	0.0362	1.2400	0.00	1.90	0.060	4.01
				0.05	0.0355	1.2400	0.06	2.00	0.056	4.34
				0.10	0.0332	1.2400	0.10	2.05	0.051	4.31
<b>C3</b>	0.05	1.75	III	0.00	0.0500	1.7284	0.00	2.87	0.054	12.67
				0.05	0.0490	1.7400	0.06	3.01	0.051	13.67
				0.10	0.0453	1.7200	0.10	3.04	0.047	12.93

**Fig. 3.** Collection of charts showing the validation of the numerical flume capabilities against the three different wave conditions with three different mean current velocities, respectively.

crest-to-trough. These two are respectively a suitable value for large 3-D simulations or the usual SPH practice for ensuring correct wave propagation [117,118].

Fig. 3 shows substantial agreement between the experimental free-surface time history and the adopted third-order wave theory (see [49, 104]), as well as the precise reproduction of the numerical solution within the SPH-based flume. Remarkably, the two adopted resolutions produce almost identical results, except for the condition C1 with  $U_0 = 0$  (panel (1,1)), in which a small loss of amplitude occurs. The latter condition features the largest steepness among the considered waves, which appears to require slightly finer SPH discretization to completely develop the target amplitude. Minor deviations can be observed, generally, for wave condition C3, when underlying currents are considered: partially laterally-skewed wave troughs appear due to the strong orbital velocities developed in the wave crest and the non-zero flow transport velocity. Additionally, it should be considered that, in spite of assuming steady wave–current interaction near the considered probes, slight disturbance may still affect the experimental measurements, as the wave is generated by a piston and only afterwards it encounters the inlet flow of the current.

Theoretical and numerical horizontal velocity profiles over depth are, instead, pictured in Fig. 4, along with a snapshot of the corresponding numerical probe placed in the middle of the wave-flume.

Three velocity profiles for each condition are paired in the three charts, respectively, depending on the underlying current velocity. Being all wave conditions characterized by intermediate depth, the bottom velocity is non-zero even in absence of current; minor divergences of the velocity values are visible near the boundary interface, as the bottom boundary is not specifically ruled by a free-slip condition. Despite the latter discrepancy and negligible numerical noise along the profiles, a common drawback for WCSPH, the velocity distribution for this wave–current field fully satisfies the engineering purposes for which this flume was developed.

### 3.4.3. Wave–Current–Structure Interaction

The proposed numerical wave tank is now validated for a floating structure. A hollow spherical buoy, 3D printed in Polyethylene Terephthalate glycol (PETG), has been placed in the CIEMito, as per Fig. 2, moored with a nylon cable in taut configuration using a small half torus. The wave conditions of Table 3 have been selected to cover Stokes' second order and third order descriptions, and to minimize sway motion of the sphere. The horizontal motion only, hence, has been captured by two cameras placed above and sideways of the sphere; surge time-history has been computed with automated video tracking procedure and averaged over the three repetitions using information

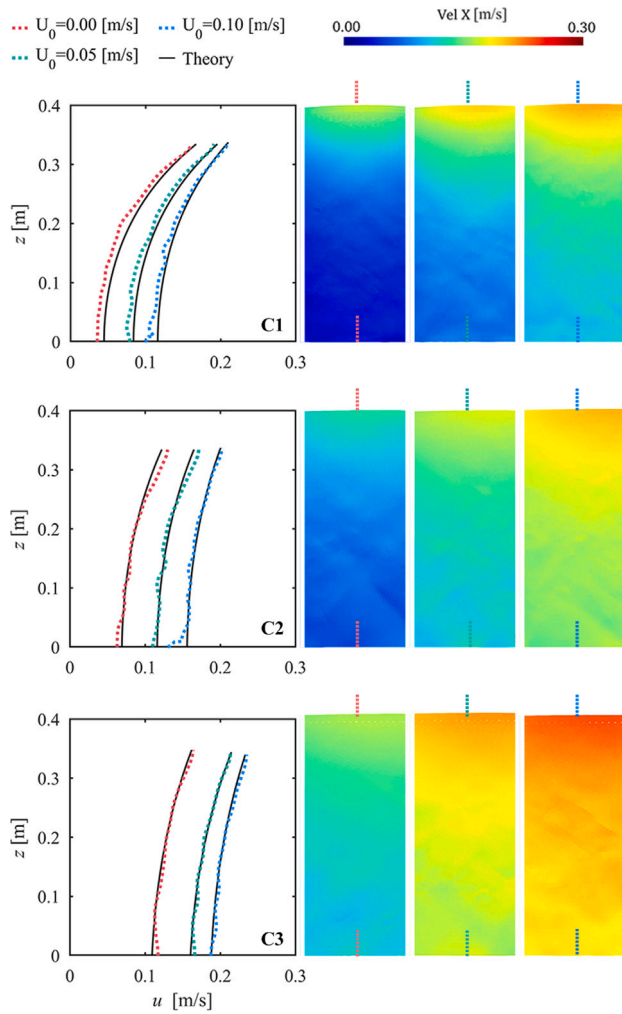


Fig. 4. Collection of charts showing the validation of the numerical flume capabilities against the three different wave conditions with three different mean current velocities, respectively.

Table 4  
Physical properties of the floating structure.

Sphere – ( $\cdot$ ) <sub>S</sub>	Material density	$\rho_S$	[kg/m <sup>3</sup> ]	1270
	Apparent density	$\rho_{S,app}$	[kg/m <sup>3</sup> ]	470.04
	Internal radius	$R_{INT}$	[m]	$2.6e^{-2}$
	External radius	$R_{EXT}$	[m]	$3.0795e^{-2}$
	Mass	$M_S$	[kg]	0.0575
Mooring – ( $\cdot$ ) <sub>M</sub>	Material density	$\rho_M$	[kg/m <sup>3</sup> ]	1140
	Nominal diameter	$D_M$	[m]	$3.50e^{-4}$
	Young modulus	$E_M$	[GPa]	0.923
	Axial stiffness	$E_M A_M$	[N]	89.79
	Still length	$l_{0,M}$	[m]	0.21805
	Number of elements	$N_M$	[–]	40

from the two cameras. The center of gravity of the sphere is considered coincident with its geometrical center, as the torus mass is neglected also in the numerical simulations. The properties of the sphere and anchoring cable are listed in Table 4. In DualSPHysics, a 3-D simulation is built up: the multipurpose numerical wave tank (Fig. 1) is laterally bounded by solid walls, 0.38-m apart, to comply with the experimental setup. The sphere is reproduced as a solid with radius  $R_{EXT}$ , density  $\rho_{S,app}$ , and mass  $M_S$ , and discretized as a set of solid SPH particles behaving according to equations mentioned in Section 2.2.1, while the anchoring line contribution is computed by MoorDynPlus (Section 2.5).

Table 5

Relative percentage error between experimental and numerical RAO values.

	C1	C2	C3
$U_0 = 0.00$ m/s	12.50%	–8.68%	0.44%
$U_0 = 0.05$ m/s	0.29%	0.19%	0.54%
$U_0 = 0.10$ m/s	5.76%	–10.30%	–5.65%

The preferred resolution for WSI validation is  $H/dp = 6$ , as it guarantees correct wave propagation and enough layers of SPH particles within the floating sphere to apply mDBC, while keeping the computational effort under control. In Fig. 5, the surge motion for wave condition C2 is compared with experimental series with increasing current velocity. Firstly, the SPH results perfectly match the experimental period regardless of the current velocity. For what concerns the motion amplitude, the agreement can be considered satisfactory up to different extents: super-imposable series can be observed for current velocity of 0.05 m/s, whereas small underestimations are found for the other two velocities. Similar behavior can be recognized for the three wave conditions in Fig. 6, which provides an overall comparison of the Response Amplitude Operator (RAO) for surge motion. The RAO is computed as the ratio of the maximum surge motion amplitude and the corresponding crest-to-trough amplitude of the incoming wave ( $H_{me}$  listed in Table 3).

As reported in Table 3, the measured wave height slightly decreases with following currents, as waves encounter the current field far from the piston. However, the interaction with currents causes a stretch in wavelength, which generally translates into larger surge amplitudes – the trend is clear for all cases except for C2 with  $U_0 = 0$ . The numerical simulations are able to capture the overall dynamics of the moored sphere, with perfect agreement on period and acceptable agreement on amplitude (maximum percentage error  $(RAO_{exp} - RAO_{num})/RAO_{exp} \approx 12\%$  – see Table 5).

However, in absence of dedicated mechanical characterization, the properties of the mooring line have been chosen among reasonable values based on generic material properties, as available literature for nylon moorings generally deals with ropes [119] and not filaments. Nylon filaments, utilized in this experiment, often present different properties in wet and dry conditions, which have not been directly quantified. The MoorDynPlus formulation, moreover, was originally developed for assessing the tension of very stiff connections with considerable mass, and generally in catenary configurations. Its lumped mass model, hence, may fail to completely capture the slight variations of tension of the present case, which may be due to the changing wave-current fields. The numerical simulations, in fact, appear dominated by the rigid mode of the structure, whereas the experimental counterpart shows more relevant participation of elastic modes.

SPH results show less sensitivity to the wavelength modification (same condition, increasing current velocities) and displaced mean position due to the constant current thrust, as the related RAO increment is likely generated by elastic elongation of the nylon connection. All in all, considering the uncertainties related to the input parameters, the results of the DualSPHysics tank testing can be considered satisfying: the proposed setup is suitable for investigating wave–structure–current interaction of moored floating structures.

#### 4. Numerical testing campaign

As further purpose of this work, we conduct a series of numerical tests on the taut-moored point-absorber Uppsala University WEC, which has relevant similarities with the structure previously tested.

We aim to recognize, with methodical use of high-fidelity tools, the unaccounted pattern in the WEC's hydrodynamics and, eventually, power yield, when the device is deployed in wave–current fields. Firstly, the numerical setup implemented in DualSPHysics by [42], built upon the experimental configuration proposed by [45,78], is validated

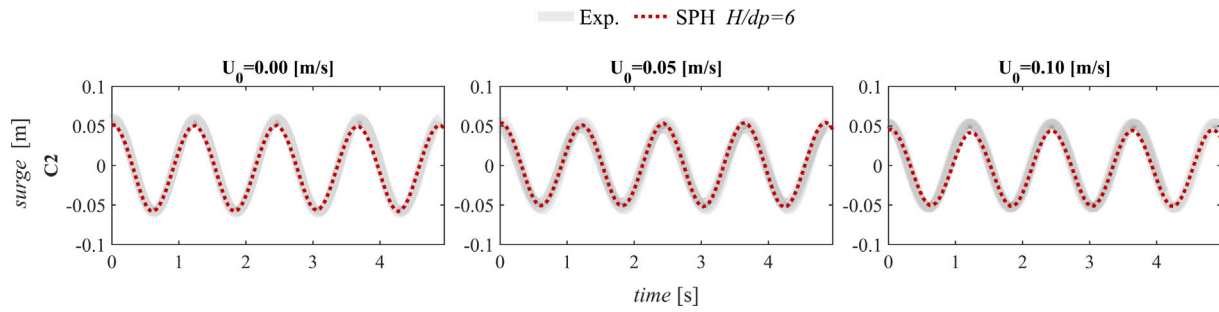


Fig. 5. Surge motion for condition C2 with three different mean current speed.

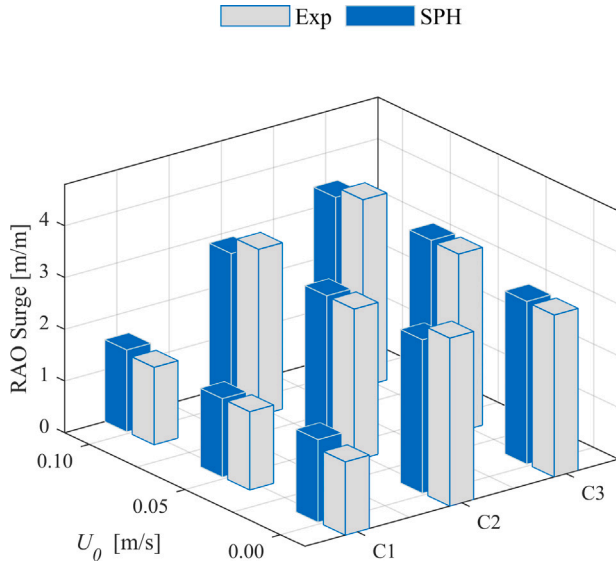


Fig. 6. Experimental and numerical Response Amplitude Operator for the surge motion of the buoy in the considered wave conditions and current speed.

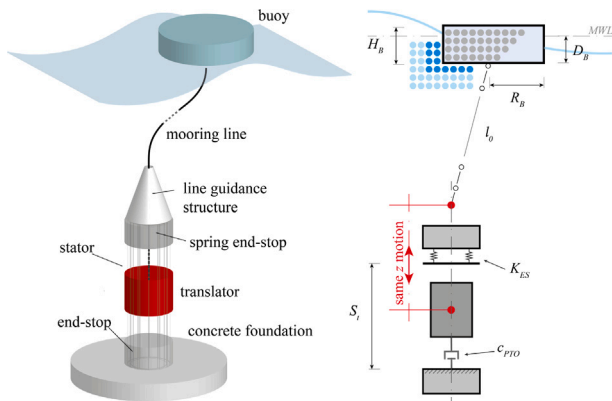


Fig. 7. Scheme of the Uppsala University WEC and its linear Power Take-Off unit (left panel), and corresponding implementation within the DualSPHysics framework (right panel).

within this novel numerical tank. Secondly, the UUWEC undergoes several tests which include different current flow velocities and directions to establish the current-modified power output over a wide spectrum of sea states.

#### 4.1. Uppsala university WEC model

A 1:20-scale (Froude similarity) for the UUWEC is herein adopted. Fig. 7 shows a simplified scheme of the UUWEC model: the motion

Table 6

Physical properties of the floating buoy, mooring line connection, and PTO system.

Buoy	Radius	$R_B$	[m]	0.085
	Draft	$D_B$	[m]	0.032
	Mass	$M_B$	[kg]	0.712
Mooring	Material density <sup>a</sup>	$\rho_M$	[kg/m <sup>3</sup> ]	1500
	Diameter <sup>a</sup>	$d_M$	[m]	$4.0 \cdot 10^{-3}$
	Unstretched length	$l_0$	[m]	2.43
	Axial stiffness	$E_M A_M$	[N]	1830
	Segments	$N_M$	[-]	40
	Weight in fluid	$W_M$	[N]	0.015
PTO System	Translator mass	$M_{PTO}$	[kg]	0.780
	Free stroke	$S_f$	[m]	0.17
	End-stop spring length	$l_{ES}$	[m]	0.030
	End-stop stiffness	$K_{ES}$	[N/m]	1940

<sup>a</sup> Plausible value that was not documented during the physical testing.

of a cylindrical buoy activates, by means of an elastic mooring line, a linear magnetic generator placed on a concrete foundation. The corresponding DualSPHysics discretization is shown aside: the buoy is discretized with SPH solid particles and interacts with fluids as per Section 2.2.1; the mooring line dynamics is managed by MoorDynPlus (Section 2.5) whereas the PTO unit is resolved using contact methods and kinematic restrictions described in Section 2.4.

In the DualSPHysics framework (right panel of Fig. 7), the anchoring point of the mooring line coincides with the center of gravity of the translator, which slides along the vertical axis according to the buoy motion and the PTO-imposed restrictions. The translator is integrated within a double end-stop system, numerically reproduced in Chrono and solved with the soft-body discrete element method (Section 2.4), whose ruling contact force is reported in Eq. (14). The upper end-stop, in addition, is attached to an elastic spring of stiffness  $K_{ES}$ , activated by the shortening of the initial spring length  $l_{ES}$  caused by the impact of the translator and the end-stop itself, which is sketched as a spring end-stop element in the setup. Rearranging Eq. (15) for the spring end-stop gives:

$$F_{ES} = K_{ES}(S_f/2 - l_{ES}). \quad (28)$$

Note that the lower end-stop, on the other hand, is fixed. The energy harvesting is represented by a damper acting as per Eq. (15), but without considering the constraint stiffness, as the sole velocity-proportional damping better represents the PTO working principles. Eq. (15) referred to the PTO damping reads:

$$F_{PTO} = c_{PTO}u_z, \quad (29)$$

where  $u_z$  is the velocity of the translator and  $c_{PTO}$  is the damping coefficient. Table 6 reports the UUWEC characteristics, including the mooring line parameters and the dimensions and features of the PTO system. The parameters defining the nature of contacts and the overall calibration procedure for the PTO are extensively detailed in [42].

In this investigation, two damping values,  $c_{PTO}$ , are considered, as previously done by [45,78]: the first one (D1) resembles a survivability

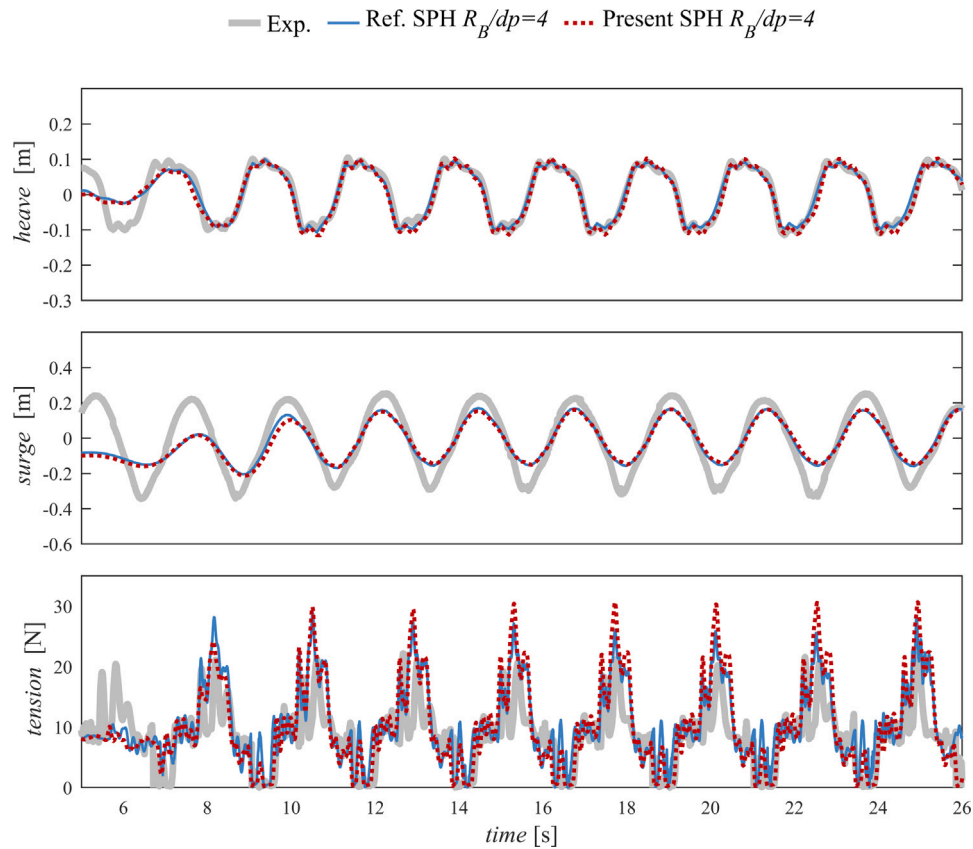


Fig. 8. Validation of the Uppsala WEC within the developed wave flume against the results proposed in [42].

Table 7

Damping definition for the two PTO configurations.

Label	Friction force		Numerical damping
	Full scale	1:20 Model	$c_{PTO}$
D1	5000 [N]	0.63 [N]	2.795 [Ns/m]
D2	59000 [N]	7.38 [N]	32.982 [Ns/m]

Table 8

Regular wave condition for the UUWEC validation.

	$T$ [s]	$H$ [m]	$d$ [m]
1:20	2.399	0.28	2.50
Full scale	10.73	5.60	50

condition, without energy harvesting purposes, whereas the second (D2) represents operational condition. According to Froude scaling procedures [120], the friction coefficient damping used in experiments and the corresponding model damping values are reported in Table 7. Condition D1 is adopted for the initial validation, whereas the operational damping D2 is implemented to evaluate the power yield of the device during the numerical testing.

#### 4.2. UUWEC validation

The proposed numerical basin has been established using numerical and experimental references from [42,78], respectively. These references feature investigations with embedded focused waves: herein, the regular pattern is solely considered, as detailed in Table 8 for model scale and corresponding full scale. The SPH resolution,  $dp$ , is parametrized with respect to the buoy radius, and set equal to  $R_B/4$  for the following simulations.

Fig. 8 depicts the heave and surge motion of the cylindrical buoy and the tension of the mooring line. The proposed setup, as expected, delivers very similar results to the reference one: heave time evolution is well captured whereas constant underestimation of surge motion affects the model response. Such deviation from the experimental series, however, has been often found in literature, even with other numerical approaches (see [45,121]), as uncertainties may directly come from experimental measurements. Moreover, the translator-mooring connection represents another source of bias between numerical and experimental models. In the physical testings, the anchoring line travels on a pulley which rectifies the final connection to the translator, whereas, in DualSPHysics, the anchoring point motion is directly shared with the translator. As such, the axis of rotation for the mooring line slightly changes according to the translator position, while in the experiments the pulley (hence the axis) is fixed and its lever arm is only defined by the line free-span.

Good agreement characterizes the tension pattern as well, with slight overestimation of the spikes for the present model. It should be noted that the SPH reference is affected by minor underestimations of the wave amplitude, which, nonetheless, can influence the measured tensions at the fairlead. With equal resolution ( $R_B/4$ ), which is relatively low in this case, the inlet boundary setup (Section 3.3.1) appears more accurate than the piston-type wavemaker adopted in [42]. However, the results are considered compliant with experimental and numerical references.

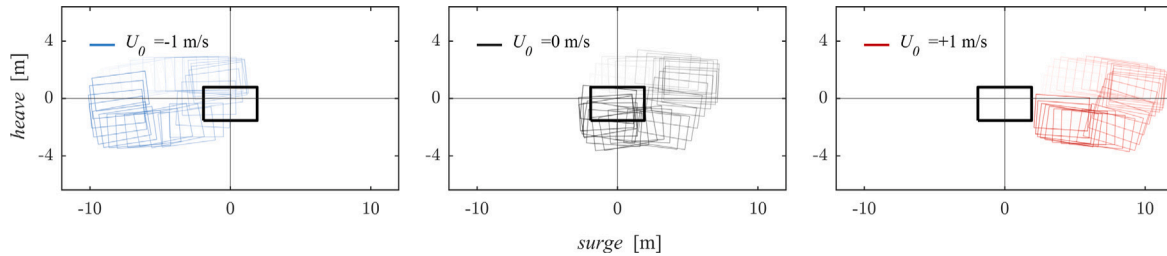
#### 4.3. Influence of underlying currents

Underlying currents are now introduced in combination with the previously validated wave condition (Table 8) to evaluate their effects on the UUWEC dynamics, adopting the exact same device configuration (PTO value D1). A range of opposing and following uniform currents spanning from  $-1.00$  m/s to  $+1.00$  m/s (values at full scale)

**Table 9**

Underlying currents simulated in DualSPHysics and corresponding scaled wave parameters for the condition of Table 8.

Full scale current [m/s]	-1.00	-0.50	-0.25	0.00	+0.25	+0.50	+1.00
$U_0$ [m/s]	-0.224	-0.112	-0.056	0.00	+0.056	+0.112	+0.224
$\lambda$ [m]	7.70	8.10	8.41	8.54	8.85	9.07	9.49
$\epsilon$ [-]	0.114	0.108	0.105	0.103	0.099	0.097	0.093

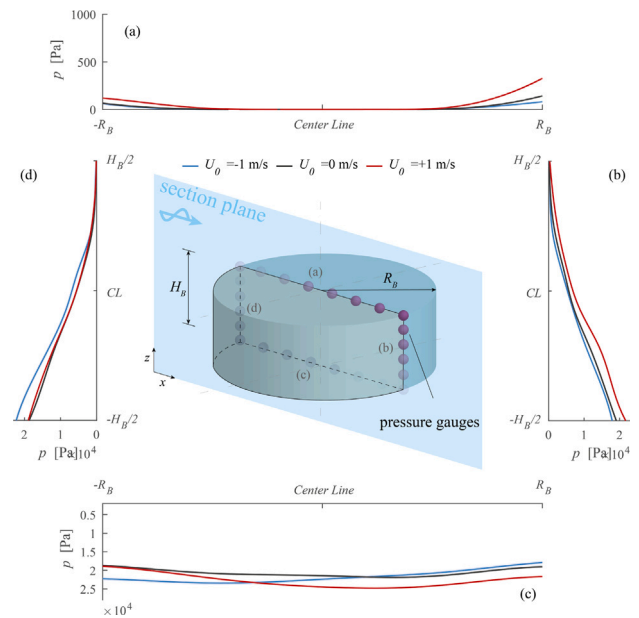
**Fig. 9.** Buoy position sequentially pictured over a wave period in the surge–heave plane for different current layouts. The black solid box centered in (0,0) represents the device rest position.

are included in the wave field. The negative sign stands for opposing current with respect to the wave propagation direction. Note that for ease of understanding, in the following charts the results are referred to full-scale current velocities values, which are chosen according to ordinary values suggested for load combinations in offshore energy design guidelines [122]. Model scale values of current speed, wavelengths, and steepness are reported in Table 9.

#### 4.3.1. Buoy's hydrodynamics

The significant hydrodynamics arising from the investigated wave–current–structure interaction problem is herein highlighted, providing useful insights to eventually characterize the device's performance. To begin with, Fig. 9 classifies the UUWEC orbital motion during a regular wave period against the current direction. The buoy position – framed at multiple instants – clearly shows the current-induced drift, which resolves into different mean equilibrium position, along with some deviation from the current-less motion pattern. Larger surge amplitudes and a relatively displaced mean position can be appreciated for opposing conditions (Fig. 9, left panel), whereas a significant drift, exacerbated by increased peak orbital velocities and relative mean velocity  $\bar{U}$ , is found for following conditions (Fig. 9, right panel). Despite the larger wavelength, the surge amplitude decreases at  $U_0 = +1$  m/s, and it is accompanied by magnified pitch angles at peak horizontal displacement, caused by coexistence of current thrust and abrupt downward force due to the end-stop engagement. Relative excess of counterclockwise pitch is caused by the  $U_0 = -1$  m/s current, which also favors wide trajectories as consequence of the larger wave steepness. The heave motion appears relatively sensitive to underlying currents: only stronger opposing currents slightly emphasize the motion at wave troughs, anyway with irrelevant magnitude.

As further perspective on the UUWEC hydrodynamic development, Fig. 10 illustrates the pressure loads on the buoy's hull during its periodic motion in the same regular wave–current field. A series of pressure gauges are attached to the buoy, distanced by half  $\Delta p$  from the boundary interface, at the intersection with the  $x-z$  plane (refer to the sketch in the central panel of Fig. 10); the wave propagation direction and an identifier for each boundary are also displayed. Local pressure values (continuous lines) are period-averaged, with shaded areas representing their standard deviation. Each point along the curve is a mean value in time, within the interval  $[0, T]$  at a fixed spatial location. Positive correlation is shown between presence of current and bottom pressure (panel (c)), with significant increase in the average load withstood by the hull during a wave period – around 15% with respect to pure wave conditions. Most notably, the highlighted divergence in pitch motion translates in an uneven redistribution of mean pressure: with following currents, associated with augmented

**Fig. 10.** Period-averaged pressures on the buoy's hull over several wave cycles, with three different current velocities — the pressure gauges are placed in the  $x-z$  plane.

clockwise rotations, the right-end side of the hull experiences, on average, increased pressure (panels (b) and (c)); in opposing currents, which cause anticlockwise rotations, the opposite behavior is observed (panels (b) and (c)).

It is worth noticing that the pitch-related loads overcome, in terms of pressure magnitude, the direct contribution of the current thrust, as the maximum load on each lateral section is achieved when the current is flowing further away from that boundary. In other words, left-hand boundary (panel (d)) presents maximum pressure with opposing currents (right-to-left); the right-hand boundary (panel (b)), instead, shows increased load with following currents (left-to-right). Panel (a) of Fig. 10 presents negligible pressure values, as overtopping phenomena are not evident in this wave condition; however, following currents appear to slightly increase the probability of partial submergence, especially when the buoy reaches the furthest horizontal position during its trajectory. In that instant, the negative tension caused by the end-stop system suddenly pulls down the buoy; with longer waves, following current may play a decisive role in exacerbate the overtopping risk for the WEC.

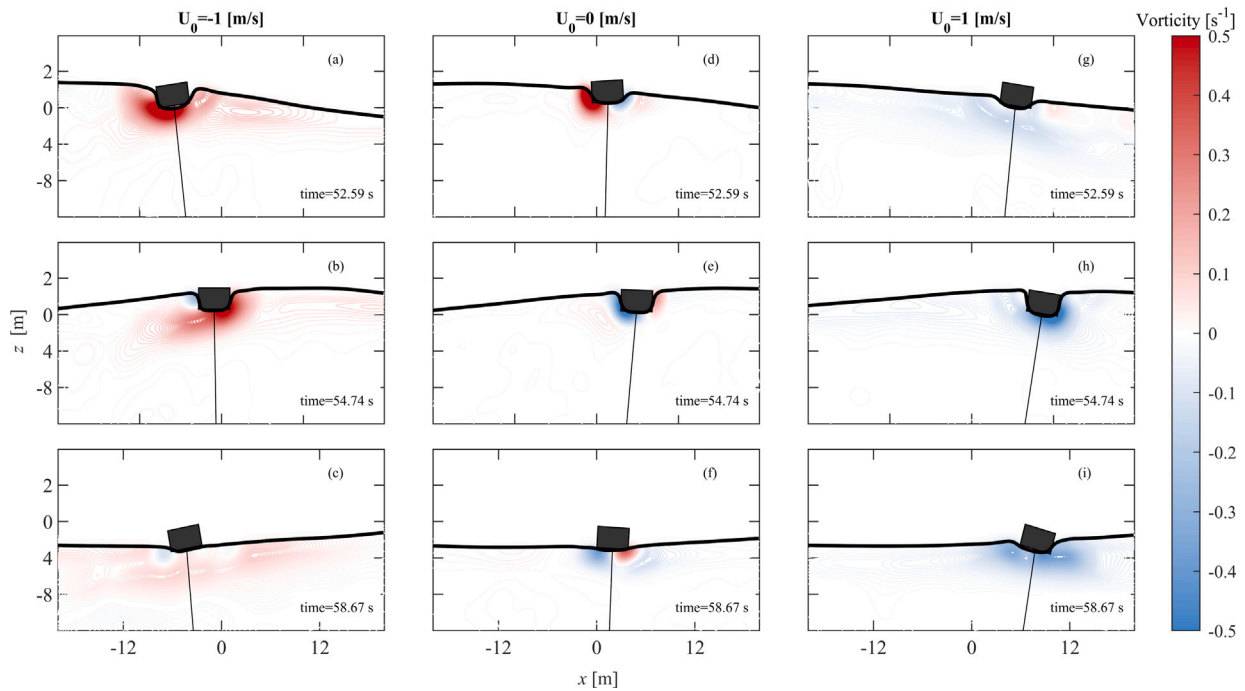


**Fig. 11.** Vorticity contour plot ( $y$ -component) in the  $x$ - $z$  plane for three different phases of wave-structure interaction and three different current speed; the thick black line individuates the free-surface.

The contour lines in Fig. 11 represent the  $y$ -component of the vorticity field at three salient instances of the wave propagation process and for the usual array of current speed. The plane  $x$ - $z$  always contains the buoy center line. Each row represents the same temporal instant, also highlighting the different wave propagation due to the Doppler-modified wavelengths, whereas every column group displays the same current layout. The vortex pattern presents recognizable dependency on the current, which clearly spreads the vorticity around the buoy and determines a predominant directionality within the velocity field. In panels (a), (b), (c), the predominant clockwise vorticity is promoted by the opposing current, flowing from right to left. Relevant vortices form around the buoy as the crest approaches (panel (a)) and the buoy offers a negative pitch angle to the head wave direction; riding the wave crest (panel (b)), predominant clockwise velocities are partially balanced by the incoming wave-generated local velocities, re-establishing a near-zero pitch for the buoy. For the current-less wave condition (panels (d), (e), (f)), symmetric vorticity develops due to the heaving buoy motion, with no significant differences between the three considered phases. Following currents, instead, introduce further non-linearities in the wave-structure interaction, as visible in panels (g), (h), (i): as the waves impacts the hull, spread counterclockwise vortices develop, further enhanced by the collinearity with wave propagation.

Overall, such hydrodynamics increases the instability of the buoy resulting in enlarged pitch angle, which in turn increase the overall load on the system (see Fig. 10, panel (c)). As visible in panel (h), moreover, the extreme surge displacement results in higher probability of overtopping, exposing the device to more challenging structural stress: high buoyancy and severe wave loads due to long wavelengths may cause swift end-stop engagements with spikes in both contact forces and mooring tensions. At wave trough, ambient currents introduce weak, but strongly directional, vorticity fields, causing tilted equilibrium positions (panels (c), (i)).

Fig. 12 concludes this hydrodynamics investigation showing the velocity field (magnitude) around the UUWEC at wave crest (top row) and trough (bottom row) from top and side perspectives. As for the previous figure, the same temporal frame yields three distinct relative wave-to-hull positions as the wavelengths varies. A recognizable trait is the current-induced wake in the velocity field, remarkable

when current and orbital velocities are partially or totally aligned (panels (a) and (e)). On the other end, for the pure wave condition, wake intensity and extension is limited (panels (c), (d)). Such current-dependent phenomenon can be of great significance for WEC arrays, adding further hydrodynamic interference within the interaction matrix; turbulent dynamics, moreover, lies outside the capabilities of low- to mid-fidelity models, as the sole radiated potential would not be able to capture the slipstream generated by the fluid flow. Through CFD-based software, instead, physical information on simplified configurations may be transferred, into the form of interaction coefficients, to light hydrodynamic or optimization models focused on array design [123].

#### 4.3.2. Absorbed power

Focusing, now, on highlighting the changes in power performance that may occur, the UUWEC is tested with operational damping (PTO configuration D2). The effects of currents are related to the translator velocity in Fig. 13, which is deduced from the corresponding element motion time-history in DualSPHysics. Along with the instant power, defined as  $c_{PTO} u_z^2$ , the surge motion (secondary  $y$ -axis) averaged over a period is also charted to better relate buoy and PTO coupled dynamics. For the sake of clarity, only the extreme values of the tested batch (i.e.,  $-1.00$  and  $+1.00$  m/s) are paired with the current-less wave condition, as they comprise, in terms of response, all other tested velocities. Heave motion representation is here discarded because no significant dependence on current has been found (see Section 4.3.1). Within the buoy dynamics previously addressed, the PTO influence is surely relevant: in Fig. 13, the surge patterns span from almost-perfect harmonics for negative  $U_0$ , to skewed irregular trajectories for positive  $U_0$ . The combination of negative current thrust and reduced wavelength keeps the generator far from the end-stops: stall positions are occupied for brief instants (see principal  $y$ -axis and PTO scheme in Fig. 13). Conversely, when the buoy is constantly displaced in the wave propagation direction and faces longer and stronger waves caused by following currents, the generator collides with the upward end-stop for longer intervals, decreasing the overall surge amplitude around the displaced equilibrium. It follows that the instant power yield presents distinguishable features as well. With  $U_0 = -1.00$  m/s,

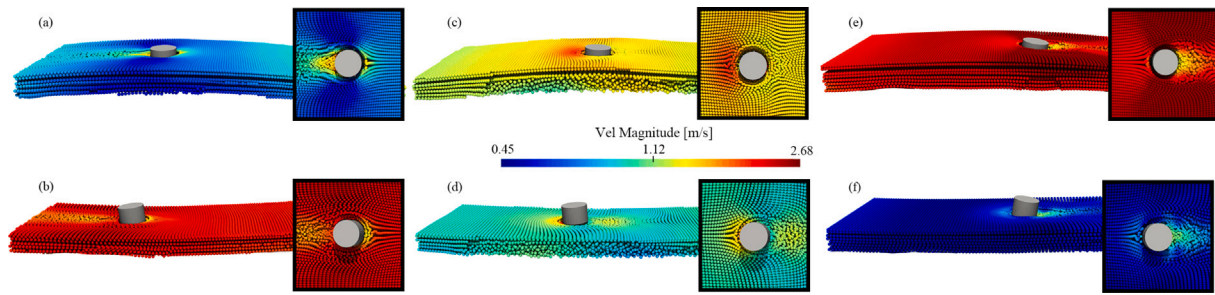


Fig. 12. Velocity magnitude around the UUWEC in a wave-current field generated with  $U_0 = [-1.00, 0.00, +1.00]$  m/s and wave parameters of Table 8; top views are added to highlight the current-generated wake.

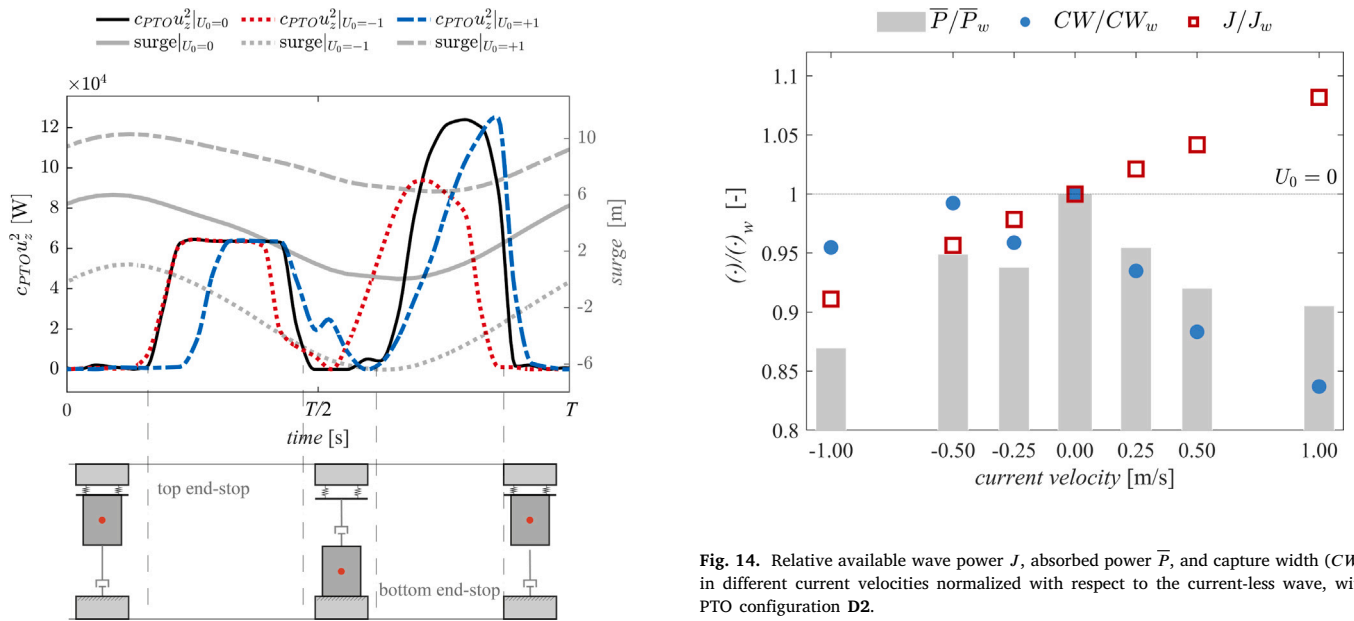


Fig. 13. Instant power delivered by the PTO unit paired with buoy surge motion for three different current flow velocities.

the instant power evolution shows mild peaks and brief stall intervals due to more regular motion patterns of the buoy. For following current ( $U_0 = +1$  m/s), instead, it counter-poses a larger spike and long-lasting operational downtime. All in all, underlying currents further increase the overall non-linearity of the UUWEC dynamics, with the PTO dynamic contribution playing a significant role when the device is engaged in the current field.

These considerations are graphically summarized in Fig. 14, featuring three performance metrics for the whole range of simulated currents: the harvested power  $\bar{P}$ , the available wave power  $J$ , and their ratio, the Capture Width  $CW = \bar{P}/J$ .  $J$  corresponds to an average energy flux for unit width in the wave propagation direction, and is computed using Eq. (18); as seen in Section 3.2, the wavenumber  $\kappa$  depends on the mean current value  $U_0$ , hence influencing the available wave power even if the total wave-current mean energy flux is disregarded accordingly to the UUWEC’s harvesting capabilities (see integral properties in Appendix A).

With a given pair  $(H, T)$ , following currents almost linearly increase the potentially harveste-able power with respect to the current-less

Fig. 14. Relative available wave power  $J$ , absorbed power  $\bar{P}$ , and capture width ( $CW$ ) in different current velocities normalized with respect to the current-less wave, with PTO configuration D2.

wave power  $J_w$ , and the vice-versa holds for opposing currents. In the same fashion, all metrics displayed in Fig. 14 are normalized with respect to the pure wave condition  $(\cdot)_w := (\cdot)|_{U_0=0}$ .  $\bar{P}$  is computed as the period-averaged instant power produced by the PTO system and reads:

$$\bar{P} = \frac{1}{T} c_{PTO} \int_0^T u_z(t)^2 dt, \quad (30)$$

As suggested by the gray bars reporting  $\bar{P}$ , for a given wave condition (Table 8), the presence of current produces a reduction in power output, worsened by high mean flow speed. This general behavior directly follows from what is shown in Fig. 13. Using the  $CW$  parameter, which quantifies the efficiency of the device, such statement can be further clarified for cases with opposing and following conditions.

- (i) With opposing currents, the available wave power decreases because of shorter wavelengths. Nonetheless, the  $CW/CW_w$  ratio remains close to unity as the contact time (time intervals in which  $u_z = 0$ ) between the generator and the end-stop is minimized. The UUWEC, thus, keeps performing as intended and harvests wave energy operating as if it were in absence of current, but facing less energetic waves. Following the reduction of  $J$ ,  $\bar{P}$  necessarily decreases.

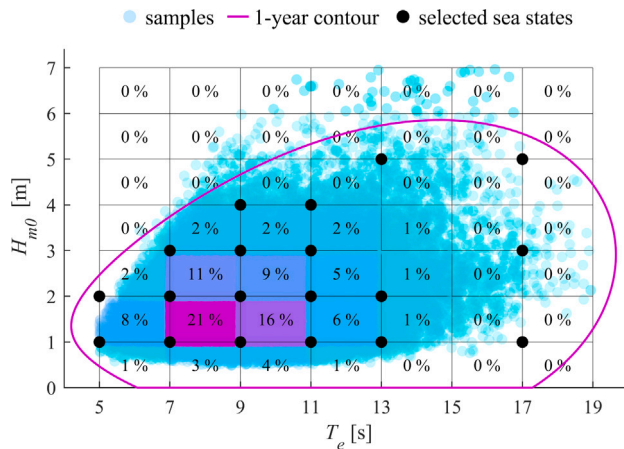


Fig. 15. Calculated sea state data from NDBC station 46026 with sea state bins based on a staggered grid ( $\Delta T_e = 2$  s,  $\Delta H_{m0} = 1$  m) and the 1-year I-FORM contour; the percentage of samples within each interval is also reported.

(ii) When following currents are included, the time span in which the translator is driven against the end-stop is directly dependent on the growing current speed, yielding reduced efficiency (losses up to the 15% of  $CW$  with respect to current-free condition). In spite of riding more energetic waves, in fact, the total device output,  $\bar{P}$ , appears akin to the one in opposing conditions.

#### 4.4. Operational conditions

The results presented in this paper, so far, show that to directly relate available wave power and theoretical output capabilities ( $CW$  is often considered constant for a device) leads to incorrect evaluation of total power production (see Fig. 14). This holds true for the tested wave condition, and keeping  $(T, H)$  unmodified when currents are introduced. To extend this outcome to a broader range of conditions, enough to evaluate the harvesting capabilities of the device in likely operational seas, a complete numerical testing campaign is carried out, using the PTO configuration **D2**. By retrieving historical spectral wave density data from the National Data Buoy Center (NDBC), station 46026, the significant wave height  $H_{m0}$  and energy period  $T_e$  are calculated using the open-source MHiT package [124]. A one-year contour is eventually identified using the modified I-FORM method [125], based on a 23-year sample of measurements. The contour is represented by the continuous purple line plotted along with the  $(H_{m0}, T_e)$  samples in Fig. 15, identifying the iso-reliability curve for the joint probability of significant wave height and energy period. To target operational conditions, the selected sea states are identified within the contour line over a staggered grid ( $\Delta T_e = 2$  s,  $\Delta H_{m0} = 1$  m). For each identified sea state (black bullets in Fig. 15), a total of five simulations are performed including the following array of current velocities:

$$U_0 = [-1.0, -0.5, 0.0, +0.5, +1.0] \text{ m/s.}$$

All tests are performed in regular waves, enough in number to achieve a steady response of the device, and with a depth of 50 m. As previously mentioned, these velocity values are adopted from the guidelines for offshore structure design (see Section 4.3); moreover, the chosen range likely includes the majority of ocean current mean speed [19] and covers ordinary tidal cycles [36]. The regular waves parameters for the sea state realizations are chosen as:

$$\begin{aligned} T &= T_e; \\ H &= H_{m0}. \end{aligned} \quad (31)$$

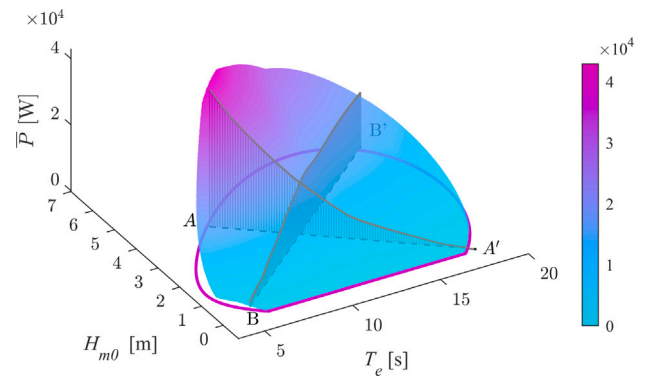


Fig. 16. Power output of the UUWEC within the considered one-year contour in absence of currents.

The following results are reported in full scale.

Lastly, it is important to report on the required resources that were run to build the processed dataset. The median computational load (sample sea state realization:  $H = 3$  m,  $T = 11$  s), as it depends on the wave-current condition simulated, is approximately 350 s per second of physical simulation on a NVIDIA Geforce RTX 4090 GPU card, running on a machine equipped with an 11th Gen Intel Core i9-11900 @ 2.50 GHz CPU unit. With this hardware, the most expensive simulation individuated from Fig. 15 ( $H = 1$  m,  $T = 17$  s) can be completed in less than 36 h. The elapsed time for the same sample simulation is roughly doubled when NVIDIA A100 GPUs from the CINECA Supercomputing center are used.

#### 4.5. Current-aware power transfer function

Using scattered data from the series of simulations (results reported in Appendix B), a power transfer function has been built via linear Delaunay triangulation, obtaining the UUWEC power output for any given  $(H, T)$  and for each current velocity  $U_0$ . The novel transfer function is defined as:

$$\mathcal{T} = \mathcal{T}(T, H, U_0),$$

with  $(T, H) \in$  one-year contour, and  $U_0$  as previously defined.

Fig. 16 reports the power yield of the UUWEC in absence of current,  $\mathcal{T}(T, H, U_0 = 0)$ , which coincides with the estimation procedure usually carried out for any WEC type. The UUWEC performs well in wave heights between 3 and 6 m and with periods between 7 and 13 s, whereas long waves and small wave heights hardly contribute to the power yield. The peak output is around 40 kW, whereas the mean output for the one-year contour is approximately 10 kW. These two figures are in line with the rated power for this particular device configuration (2-m buoy radius) as proposed in [123].

To highlight the influence of currents in the most efficient sea state range, Fig. 17 reports details of the  $T_e = [6, 11]$  s -  $H_{m0} = [3, 5]$  m range. Coherently with what has been observed during the preliminary investigation on experimental waves (Fig. 14), the sole introduction of current reduces the device performance, regardless. Extreme current values strongly hamper the power yield of the UUWEC, as moderate currents do to a lesser extent. The closest performance with respect to the current-less field is achieved when  $U_0 = 0.50$  m/s, for which still holds an acceptable balance between available power and operational downtime for the PTO.

In Fig. 16, the position of the two section planes are sketched to enhance the readability of the current-aware transfer function. These planes are used to examine the evolution of the power absorption

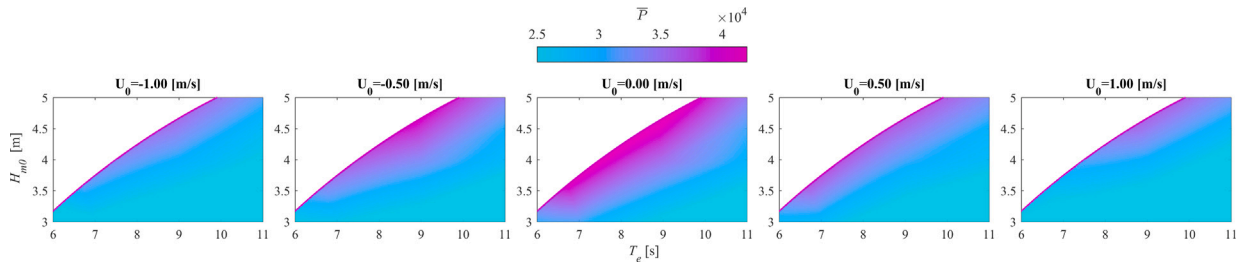


Fig. 17. Detail of the most energetic zone of the power output surface for the five considered current velocities.

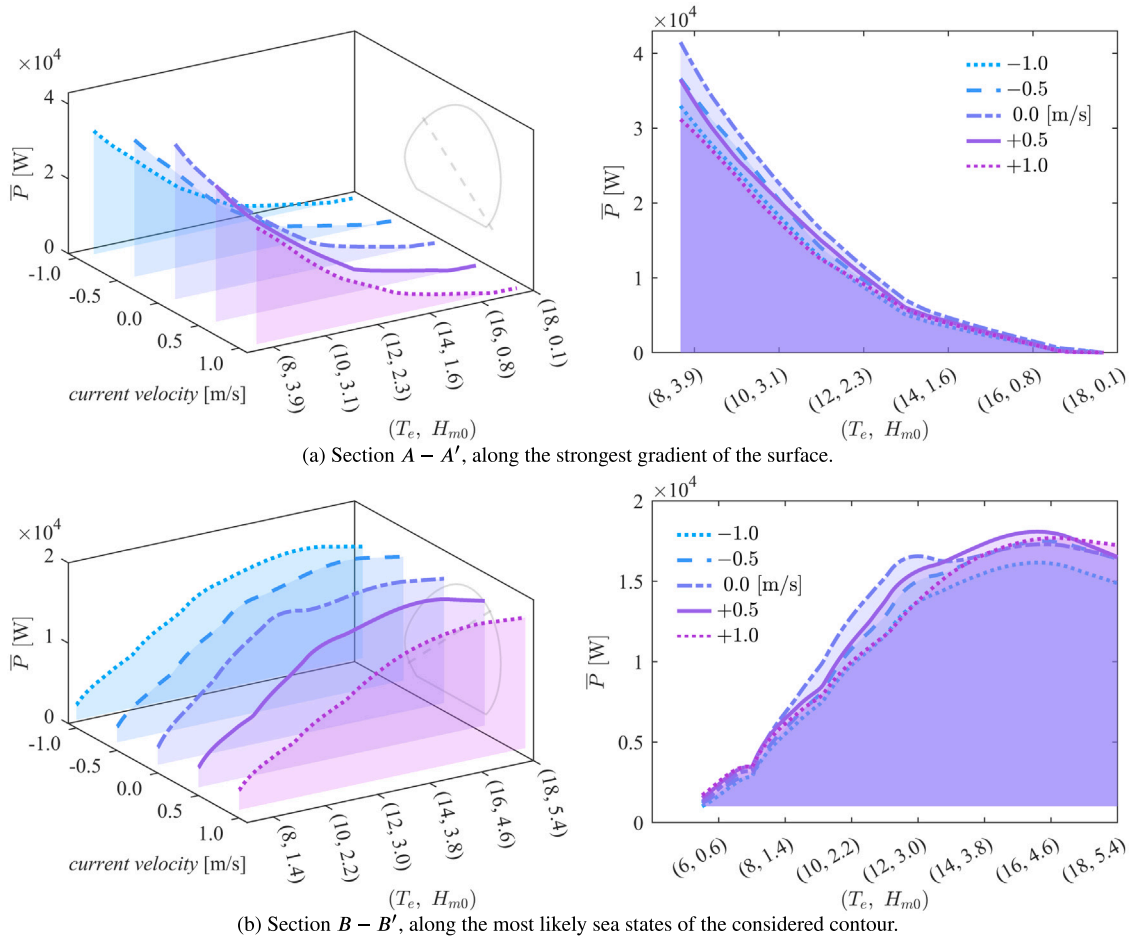


Fig. 18. Sections of the five different power output surfaces depending on the underlying current value.

capabilities depending on the current features. A cross-section for each value of current is reported in Fig. 18, depicting slices  $A-A'$  and  $B-B'$ . These charts report the period–wave height pair on the horizontal axis and absorbed power on the vertical axis. Fig. 18(a) roughly follows the strongest surface gradient, clearly highlighting the current-dependent power output. With optimal conditions, a following current of 1.00 m/s can cost up to 25% of the harnessed power. For relative short periods and wave heights around 3.00 m, in fact, the strong difference in magnitude between orbital velocities and phase velocity, amplifies the effects shown in Section 4.3, enlarging stall intervals for the generator. Section  $B-B'$ , instead, covers the more likely sea state bins, within

which the current-less environment still delivers the best performance ( $7 < T_e < 11$  s,  $1 < H_{m0} < 3$  m). In Fig. 18(b), nonetheless, beneficial effects for long waves–following current combination ( $T_e > 13$  s) can be appreciated: in this case, the highly energetic content and longer wavelengths translates into slightly enhanced power production. However, the probability of such conditions can be from slim to none.

To further summarize and provide a clearer estimate of the results, the yearly power matrix for the device based on the current-aware transfer function  $\mathcal{T}$  is plotted in Fig. 19 using sea-state data as per Fig. 15. Each bin reports the one-year power production based on the probability of occurrence of the included sea states, based upon

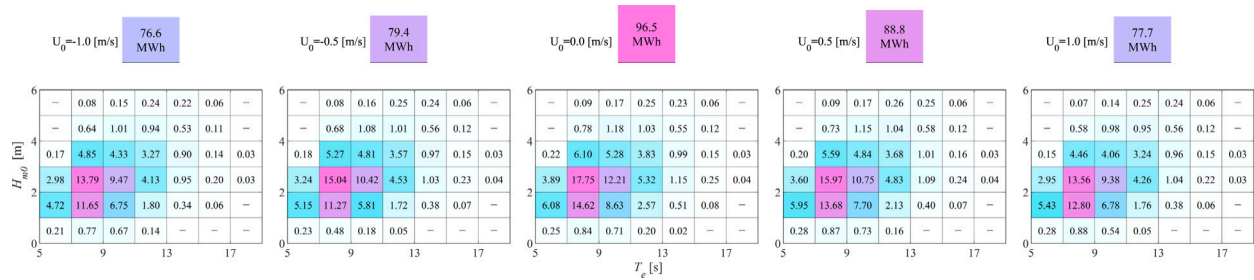


Fig. 19. One-year power matrix of the UUWEC applying a current-aware transfer function to the wave data available from NDBC station 46 026, considering the current condition constant for the whole period.

23 years of measurements. The matrices consider a constant value of current for the entire time interval, and the total annual power yield is reported in the panel above (all quantities in MWh). The reported information can be combined, if current measurements are available along with spectral wave data, to realistically recreate the power output of the UUWEC in a wave–current environment. For instance, considering 0.5 m/s as average value of current, a yearly power drop of around 10% is to be expected.

This broad analysis conducted on a representative ocean environment, hence, confirms tangible deviation from standard wave-only performance when underlying currents are considered. Strong currents can severely jeopardize the UUWEC power output near its resonant conditions, whereas negligible improvements are obtained for very long waves and mild current velocities. Nevertheless, both power yield and likelihood of such conditions ( $T_e > 14$  s,  $H_{m0} > 4$  m) relegate the latter occurrence to a secondary role in the overall performance evaluation.

## 5. Conclusions

In this work, a systematic numerical approach to investigate floating device dynamics in realistic marine environments, or rather waves and current combinations, has been proposed, validated, and applied to a point-absorber wave energy converter. This numerical tank is suitable for testing highly-dynamic marine structures, as it is developed in the DualSPHysics framework, which, along with SPH inherent capabilities, employs a coupling with Chrono to reproduce mechanical systems, and with MoorDynPlus to mimic anchoring connections.

With the use of ad-hoc developed open boundary conditions and finely tuned passive absorption, the numerical tank efficiently reproduces the combination of high-order waves and uniform currents, while guaranteeing the sufficient flexibility to host light floating structures. Within this novel basin, an extensive investigation into the dynamics, and eventually performance modification experienced by the Uppsala University WEC in wave–current fields has been carried out. Starting from a single wave condition and extending the survey to representative operational sea states, current's magnitude and orientation effects on the buoy's hydrodynamics have been clarified, and their consequences on the power yield of the device comprehensively addressed.

The principal outcomes of this investigation can be summarized as follows:

- Current action can significantly alter point-absorber WECs hydrodynamics. Pressure, vorticity, and velocity fields around the buoy show strong correlation with currents layout, promoting, in combination with the mechanical constraints offered by power take-off systems, the development of system non-linearity. As the data suggests, the PTO configuration strongly influences the overall structure response, as current flow shifts it towards complex motion patterns even when the wave parameters themselves are not particularly demanding.

- Underlying currents can potentially hamper the power production of point-absorber devices. For following currents (i.e., parallel to the wave propagation field), the UUWEC efficiency was greatly reduced, exposing the considered design to its limits, whereas opposing currents (i.e., anti-parallel to the wave propagation field) reduced the available wave power for a given pair of ( $T$ ,  $H$ ). At peak power production, strong currents can cut the power yield down by up to 25% with respect to pure wave environments (Fig. 18(a)). On a yearly basis, considering the constant current contribution, the UUWEC harnesses between 7 and 20% less, depending on the mean flow velocity and direction (Fig. 19).

As such, even during early design stages, a deepened understanding of the environmental conditions and structure response can significantly determine the development of a certain concept, as current action poses non-negligible menaces to the ongoing design practices, both in terms of preliminary performance estimation and dimensioning. On account of the previous considerations, this work provides the following insights:

- When estimating power in wave–current fields, the sole modification of the available wave power via spectral components can be misleading and could potentially further divert the predicted power production from the real one. A *current-aware* transfer function is believed necessary to take into account the complete hydrodynamics and consequent PTO performance, as the device power matrix significantly varies in the three-dimensional space of ( $T$ ,  $H$ ,  $U_0$ ).
- If currents of relevant magnitudes are among the site-specific conditions, the overall design of the device, and specially its PTO unit, should undergo a dedicated sizing process. Via adopting passive (e.g., stroke length, anchoring line characteristics) or active (e.g., damping control) strategies, the WEC harnessing capabilities can be optimized to draw efficiently from the available wave power; oceanic currents and tidal currents, due to their different magnitudes and features, may require different treatments, prioritizing passive or active solution, respectively.
- Combination of regular waves and steady uniform currents are suitable environmental descriptions for CFD models, and can represent, at small approximation costs, also depth-dependent currents [126]. The higher computational cost of CFD simulations with respect to so-called engineering tools is justified for operational conditions that feature overlooked complexity, as the one herein tackled. High-fidelity tools are definitely recommendable not only for harsh sea states, but whenever the fluid–structure aggregate presents relevant non-linearity and unforeseeable second-order effects.

This work lays the basis for more conscious treatment of the wave–current problem for dynamic wave energy converters, offering deepened perception of underlying physics and general working principles.

The current-aware transfer function is a powerful instrument to match acquired ocean data including current measurements, or synthetic data generated with wave–current propagation models, with realistic power output drawn from a comprehensive physical modeling of the sea state.

Future work will focus on augmenting ongoing power assessment of WECs with physically-based response functions in realistic environments. The impact of underlying currents could be exponentially amplified on larger scales, as for WEC farms [127]. Apart from individual performance of each device, the modified hydrodynamics could play a significant role in energy park design. The overarching objective, in this regard, would be to host multiple devices within the high-fidelity basin [128] and to extend the relevant working principles to existing optimization techniques (see [123,129,130]). Besides, the developed basin can also be applied to different floating structures, for which current loads and modified wave parameters can be worth investigating: floating wind platforms are of certain interest, and already validated in the same numerical framework [64,65,67], as well as visco-elastic floating covers (very large floating structures, flexible floating solar systems) for which DualSPHysics offers valuable modeling options [98,131,132].

### CRedit authorship contribution statement

**Salvatore Capasso:** Writing – original draft, Visualization, Validation, Software, Methodology, Investigation, Formal analysis, Data curation, Conceptualization. **Bonaventura Tagliaferro:** Writing – review & editing, Writing – original draft, Methodology, Investigation, Formal analysis, Conceptualization. **Iván Martínez-Estévez:** Writing – review & editing, Software, Investigation. **Corrado Altomare:** Writing – review & editing, Resources, Methodology. **Moncho Gómez-Gesteira:** Writing – review & editing, Supervision, Methodology, Formal analysis, Conceptualization. **Malin Göteman:** Writing – review & editing, Supervision, Methodology, Conceptualization. **Giacomo Viccione:** Writing – review & editing, Supervision, Resources, Project administration, Methodology, Funding acquisition.

### Declaration of competing interest

The authors declare that they have no known competing financial interests or personal relationships that could have appeared to influence the work reported in this paper.

### Data availability

Data will be made available on request.

### Acknowledgments

S. Capasso gratefully acknowledges Prof. B. Rogers for the valuable discussions, and the University of Manchester for hosting his research stay. The authors acknowledge the insightful comments provided by Prof. A.J.C. Crespo (University of Vigo, Spain) and Dr. J.M. Domínguez (University of Vigo, Spain). We acknowledge the CINECA award under the ISCRA initiative, for the availability of high-performance computing resources and support. S. Capasso acknowledges fundings from WECANet COST Action CA17105 “A pan-European Network for Marine Renewable Energy with a Focus on Wave Energy” supporting a STSM at the Universitat Politècnica de Catalunya – BarcelonaTech. We are grateful for the computing resources from the Northern Ireland High Performance Computing (NI-HPC) service funded by EPSRC, UK (EP/T022175). M. Göteman and B. Tagliaferro acknowledge the support provided by the National Academic Infrastructure for Super-computing in Sweden (NAISS) through the project NAISS 2023/5-351 for the use of the GPU partition Tetralith2 at the National Supercomputer Centre (NSC). I. Martínez-Estévez acknowledges funding from Xunta de Galicia under “Programa de axudas

**Table 10**  
Coefficients for third order Stokes solution of Eqs. (23) and (24).

$a_1 = H/2$
$a_2 = 1/4\kappa a_1^2 \left( \frac{2+\cosh 2\kappa d}{\sinh \kappa d^2} \right) \cosh \kappa d$
$a_3 = 3/64\kappa^2 a_1^3 \left( \frac{1+8\cosh \kappa d^6}{\sinh \kappa d^6} \right)$
$\omega_R = \sqrt{\kappa g \tanh(\kappa d)} \left( 1 + (\kappa a_1)^2 \frac{8+\cosh 4\kappa d}{8 \sinh \kappa d^2} \right)^{1/2}$
$A_0 = U_0$
$A_1 = a_1 \omega_R \frac{\cosh \kappa(z+d)}{\kappa \sinh \kappa d}$
$A_2 = \frac{3}{8} a_1^2 \omega_R \frac{\cosh 2\kappa(z+d)}{\sinh \kappa d^2}$
$A_3 = \frac{1}{64} a_1^3 \omega_R \kappa \left( \frac{11-2\cosh 2\kappa d}{\sinh \kappa d^2} \right) \cosh 3\kappa(z+d)$

á etapa predoutoral da Consellería de Cultura, Educación e Universidades da Xunta de Galicia” (ED481A-2021/337). This work was partially supported by the project SURVIWEC PID2020-113245RB-I00 financed by MCIN/AEI/10.13039/501100011033 and by the project ED431C 2021/44 “Programa de Consolidación e Estructuración de Unidades de Investigación Competitivas” financed by Xunta de Galicia, Consellería de Cultura, Educación e Universidade, Spain. Grant TED2021-129479A-I00 funded by Ministerio de Ciencia e Innovación (MCIN/AEI/10.13039/501100011033) and by the “European Union NextGenerationEU/PRTR”. Dr. Corrado Altomare acknowledges funding from the Spanish government and the European Social Found (ESF) under the programme “Ramón y Cajal 2020” (RYC2020-030197-I/AEI/10.13039/501100011033).

### Appendix A. Integral wave properties

In this section, we complete the theoretical description of the wave–current problem. The coefficients of the Stokes solution for the wave–current velocity field and free-surface elevation up to the third order are given in Table 10.

Furthermore, the integral wave properties as obtained by [24,133] are reported. Among them, it is relevant to consider the wave-related power  $J$  in presence of current (Eq. (18)) and the total wave–current mean energy flux  $F$ , that is:

$$F = c(3E_k - 2E_p) + \frac{1}{2}u_b^2(I_w + \rho c d) - 2cU_0I_w \quad (32)$$

In the above equation:

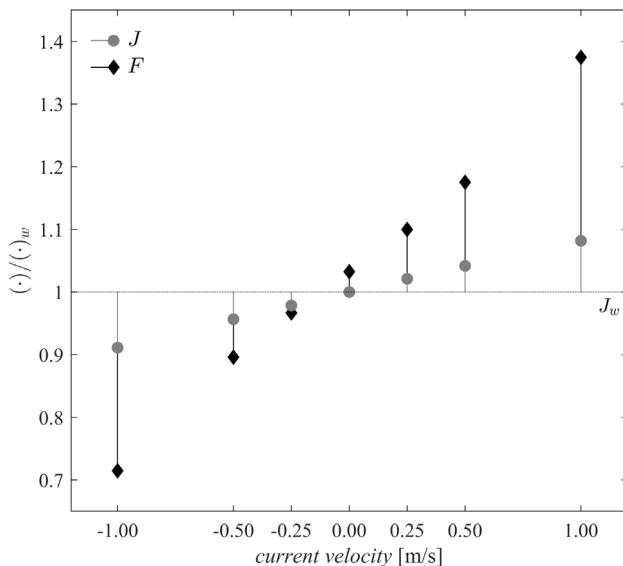
$$\begin{aligned} E_k &= \frac{1}{2}(cI_w - U_0Q), \\ E_p &= \frac{1}{4}\rho\left(\frac{g}{I_w\kappa^2}\right)\epsilon^2(1 - 2\epsilon^2C_0D_4), \\ I_w &= \int_0^\eta \rho u dz = \rho U_2 d, \\ Q &= \rho d(\bar{U} - U_{ret}), \\ U_{ret} &= \sqrt{\frac{g}{\kappa}} \left( \epsilon^2 \frac{(-\coth \kappa d^2)}{2\kappa d} \right), \\ R &= \frac{g}{\kappa} \left( \frac{C_0^2}{2} + E_2\epsilon^2 \right), \\ u_b^2 &= 2R - c(c - 2U_0), \\ D_4 &= (\coth \kappa d)^{1/2} (2 + 4S + S^2 + 2S^3)/(8(1 - S)^3), \\ E_2 &= \tanh \kappa d (2 + 2S + 5S^2)/(4(1 - S)^2). \end{aligned}$$

$E_k$  and  $E_p$  are the kinetic and potential energy per unit horizontal area, respectively;  $I_w$  is the mean mass flux in the fixed frame of reference, and  $Q$  the mean mass flux in the moving frame of reference (see Section 3.2).  $U_{ret}$  is the return current,  $R$  is the Bernoulli constant and  $u_b$  is the horizontal velocity at bottom.  $D_4$  and  $E_2$  are coefficients drawn from Fenton’s fifth order Stokes solution [112].

Fig. 20 depicts the comparison between  $F$  and  $J$  for the condition reported in Table 8, considering the usual array of current values. According to the WEC features, the contribution of the current to

**Table 11**Power absorption results for the considered sea states reported in Fig. 15, and corresponding  $(T, H)$  pair; all results in kW.

$U_0$ [m/s]	ST1 (5,1)	ST2 (7,1)	ST3 (9,1)	ST4 (11,1)	ST5 (13,1)	ST6 (17,1)	ST7 (7,2)	ST8 (9,2)	ST9 (11,2)	ST10 (13,2)	ST11 (7,3)	ST12 (9,3)	ST13 (11,3)	ST14 (17,3)	ST15 (11,4)	ST16 (13,5)	ST17 (17,5)	ST18 (5,2)	ST19 (9,4)	ST20 (11,5)
-1.00	2.42	2.84	2.43	1.75	1.07	0.29	10.58	8.52	6.49	5.23	23.46	19.46	14.97	7.24	24.56	25.03	15.55	10.45	29.45	30.94
-0.50	2.99	2.88	2.43	1.97	1.54	0.64	11.44	9.23	7.24	5.76	25.45	21.77	16.49	8.52	27.67	26.27	17.00	13.25	33.35	33.14
0.00	3.29	3.11	2.32	1.72	1.59	0.95	13.78	11.41	9.34	7.23	30.63	23.89	19.09	8.55	29.08	25.54	16.94	16.02	35.56	34.55
+0.50	3.98	3.41	2.55	1.97	1.39	0.23	13.13	9.65	7.85	6.20	27.70	21.02	17.64	8.95	27.10	27.46	17.34	16.21	30.89	33.31
+1.00	4.53	3.42	2.76	2.03	1.30	0.17	11.97	8.96	7.50	5.99	21.40	18.04	14.34	7.83	22.67	26.46	17.51	16.68	29.25	30.94

**Fig. 20.** Available wave power considering current flux ( $F$ ) and without considering current flux ( $J$ ) normalized with respect to the current-less wave power ( $J_w$ ) for the wave condition Table 8.

the energy flux is disregarded; its evaluation would have significantly decreased the relative capture width gauge utilized in Fig. 14. The traditional wave power definition is used instead (Eq. (18)), including the current-modified wavenumber within the group velocity term.

## Appendix B. Operational sea state numerical results

In Table 11, the power output value for each simulated sea state is provided, listed per current flow velocity.

## References

- [1] Cruz J. Ocean wave energy: current status and future perspectives. 1st ed.. Berlin, Germany: Springer Berlin, Heidelberg; 2008. <http://dx.doi.org/10.1007/978-3-540-74895-3>.
- [2] Khan N, Kalair A, Abas N, Haider A. Review of ocean tidal, wave and thermal energy technologies. *Renew Sustain Energy Rev* 2017;72:590–604. <http://dx.doi.org/10.1016/j.rser.2017.01.079>, URL <https://www.sciencedirect.com/science/article/pii/S1364032117300965>.
- [3] Reguero B, Losada I, Méndez F. A global wave power resource and its seasonal, interannual and long-term variability. *Appl Energy* 2015;148:366–80. <http://dx.doi.org/10.1016/j.apenergy.2015.03.114>, URL <https://www.sciencedirect.com/science/article/pii/S030626191500416X>.
- [4] Rusu L, Onea F. The performance of some state-of-the-art wave energy converters in locations with the worldwide highest wave power. *Renew Sustain Energy Rev* 2017;75:1348–62. <http://dx.doi.org/10.1016/j.rser.2016.11.123>, URL <https://www.sciencedirect.com/science/article/pii/S1364032116308838>.
- [5] Coe RG, Bacelli G, Forbush D. A practical approach to wave energy modeling and control. *Renew Sustain Energy Rev* 2021;142:110791. <http://dx.doi.org/10.1016/j.rser.2021.110791>, URL <https://www.sciencedirect.com/science/article/pii/S1364032121000861>.
- [6] Paduano B, Parrinello L, Niosi F, Dell'Edera O, Sirigu SA, Faedo N, Mattiazzo G. Towards standardised design of wave energy converters: A high-fidelity modelling approach. *Renew Energy* 2024;224:120141. <http://dx.doi.org/10.1016/j.renene.2024.120141>, URL <https://www.sciencedirect.com/science/article/pii/S0960148124002064>.
- [7] Karimirad M, Jiang Z. 2.08 - Mechanical-dynamic loads. In: Letcher TM, editor. *Comprehensive renewable energy* (second edition). 2nd ed.. Oxford: Elsevier; 2022, p. 194–225. <http://dx.doi.org/10.1016/B978-0-12-819727-1.00075-3>, URL <https://www.sciencedirect.com/science/article/pii/B9780128197271000753>.
- [8] Mattiazzo G. State of the art and perspectives of wave energy in the mediterranean sea: Backstage of ISWEC. *Front Energy Res* 2019;7. <http://dx.doi.org/10.3389/fenrg.2019.00114>, URL <https://www.scopus.com/inward/record.uri?eid=2-s2.0-85075249921&doi=10.3389%2ffenrg.2019.00114&partnerID=40&md5=51333ba047bc3dfbad57664ebda757d7>.
- [9] Guo C, Sheng W, De Silva DG, Aggidis G. A review of the leveled cost of wave energy based on a techno-economic model. *Energies* 2023;16(5). <http://dx.doi.org/10.3390/en16052144>, URL <https://www.scopus.com/inward/record.uri?eid=2-s2.0-85149724157&doi=10.3390%2fen16052144&partnerID=40&md5=e1534142664f3bc22a4db64822961d7a>.
- [10] Coe RG, Ahn S, Neary VS, Kobos PH, Bacelli G. Maybe less is more: Considering capacity factor, saturation, variability, and filtering effects of wave energy devices. *Appl Energy* 2021;291:116763. <http://dx.doi.org/10.1016/j.apenergy.2021.116763>, URL <https://www.sciencedirect.com/science/article/pii/S0306261921002701>.
- [11] Xu S, Wang S, Guedes Soares C. Review of mooring design for floating wave energy converters. *Renew Sustain Energy Rev* 2019;111:595–621. <http://dx.doi.org/10.1016/j.rser.2019.05.027>, URL <https://www.sciencedirect.com/science/article/pii/S1364032119303399>.
- [12] Zhang L, Shi W, Karimirad M, Michailides C, Jiang Z. Second-order hydrodynamic effects on the response of three semisubmersible floating offshore wind turbines. *Ocean Eng* 2020;207:107371. <http://dx.doi.org/10.1016/j.oceaneng.2020.107371>, URL <https://www.sciencedirect.com/science/article/pii/S0029801820304029>.
- [13] Shi W, Zhang L, Karimirad M, Michailides C, Jiang Z, Li X. Combined effects of aerodynamic and second-order hydrodynamic loads for floating wind turbines at different water depths. *Appl Ocean Res* 2023;130. <http://dx.doi.org/10.1016/j.apor.2022.103416>, URL <https://www.scopus.com/inward/record.uri?eid=2-s2.0-85142524500&doi=10.1016%2fj.apor.2022.103416&partnerID=40&md5=3905fa85225db9f2d925a92ad8e10548>.
- [14] Niosi F, Begovic E, Bertorello C, Rinauro B, Sannino G, Bonfanti M, Sirigu S. Experimental validation of orcaflex-based numerical models for the PEWEC device. *Ocean Eng* 2023;281. <http://dx.doi.org/10.1016/j.oceaneng.2023.114963>, URL <https://www.scopus.com/inward/record.uri?eid=2-s2.0-85161684486&doi=10.1016%2fj.oceaneng.2023.114963&partnerID=40&md5=bf8487c0865d525aa9e1a3c1929f2d3e>. Cited by: 3.
- [15] Clemente D, Rosa-Santos P, Taveira-Pinto F. Numerical developments on the E-motions wave energy converter: Hull design, power take-off tuning and mooring system configuration. *Ocean Eng* 2023;280. <http://dx.doi.org/10.1016/j.oceaneng.2023.114596>, URL <https://www.scopus.com/inward/record.uri?eid=2-s2.0-85153221913&doi=10.1016%2fj.oceaneng.2023.114596&partnerID=40&md5=ca8586018d608ab4e9c31efae55f9880>. Cited by: 0; All Open Access, Hybrid Gold Open Access.
- [16] Windt C, Davidson J, Ringwood JV. High-fidelity numerical modelling of ocean wave energy systems: A review of computational fluid dynamics-based numerical wave tanks. *Renew Sustain Energy Rev* 2018;93:610–30. <http://dx.doi.org/10.1016/j.rser.2018.05.020>, URL <https://www.sciencedirect.com/science/article/pii/S1364032118303629>.
- [17] Zeng X, Shao Y, Feng X, Xu K, Jin R, Li H. Nonlinear hydrodynamics of floating offshore wind turbines: A review. *Renew Sustain Energy Rev* 2024;191:114092. <http://dx.doi.org/10.1016/j.rser.2023.114092>, URL <https://www.sciencedirect.com/science/article/pii/S1364032123009504>.
- [18] Fratantoni DM. North atlantic surface circulation during the 1990's observed with satellite-tracked drifters. *J Geophys Res: Oceans* 2001;106(C10):22067–93.
- [19] Tolman HL. The influence of unsteady depths and currents of tides on wind-wave propagation in shelf seas. *J Phys Oceanogr* 1990;20:1166–74, URL <https://api.semanticscholar.org/CorpusID:129572520>.

- [20] Lorente P, Piedracoba S, Sotillo MG, Álvarez Fanjul E. Long-term monitoring of the atlantic jet through the strait of gibraltar with HF radar observations. *J Mar Sci Eng* 2019;7(1). <http://dx.doi.org/10.3390/jmse7010003>, URL <https://www.scopus.com/inward/record.uri?eid=2-s2.0-85060241890&doi=10.3390/jmse7010003&partnerID=40&md5=e35223a9598569249ccc39a9e32c2d22>.
- [21] Rapizo H, Durrant TH, Babanin AV. An assessment of the impact of surface currents on wave modeling in the southern ocean. *Ocean Dyn* 2018;68(8):939–55.
- [22] Wolf J, Prandle D. Some observations of wave–current interaction. *Coast Eng* 1999;37(3):471–85. [http://dx.doi.org/10.1016/S0378-3839\(99\)00039-3](http://dx.doi.org/10.1016/S0378-3839(99)00039-3), URL <https://www.sciencedirect.com/science/article/pii/S0378383999000393>.
- [23] Dean RG, Dalrymple RA. *Water wave mechanics for engineers and scientists*. World Scientific; 1991. <http://dx.doi.org/10.1142/1232>, arXiv:<https://www.worldscientific.com/doi/abs/10.1142/1232>. URL <https://www.worldscientific.com/doi/abs/10.1142/1232>.
- [24] Fenton J. *Nonlinear wave theories*. In: MéHauté BL, Hanes D, editors. *The sea*, vol. 9: ocean engineering science. New York: Wiley; 1990.
- [25] Baddour R, Song S. Interaction of higher-order water waves with uniform currents. *Ocean Eng* 1990;17(6):551–68. [http://dx.doi.org/10.1016/0029-8018\(90\)90023-Y](http://dx.doi.org/10.1016/0029-8018(90)90023-Y).
- [26] Song Z-y, Zhao H, Li L, Lü G. On the universal third order Stokes wave solution. *Sci China Earth Sci* 2012;56. <http://dx.doi.org/10.1007/s11430-012-4523-z>.
- [27] Zhao K, Liu PLF. On Stokes wave solutions. *Proc R Soc Lond Ser A* 2022;478(2258):20210732. <http://dx.doi.org/10.1098/rspa.2021.0732>.
- [28] Jonsson IG. *Wave-current interactions*. Sea 1990;9:65–120.
- [29] Peregrine D. In: Yih C-S, editor. *Interaction of water waves and currents*. Advances in applied mechanics, vol. 16, Elsevier; 1976, p. 9–117. [http://dx.doi.org/10.1016/S0065-2156\(08\)70087-5](http://dx.doi.org/10.1016/S0065-2156(08)70087-5), URL <https://www.sciencedirect.com/science/article/pii/S0065215608700875>.
- [30] Thomas GP. Wave-current interactions: an experimental and numerical study. Part 1. Linear waves. *J Fluid Mech* 1981;110:457–74. <http://dx.doi.org/10.1017/S0022112081000839>.
- [31] Thomas GP. Wave–current interactions: an experimental and numerical study. Part 2. Nonlinear waves. *J Fluid Mech* 1990;216:505–36. <http://dx.doi.org/10.1017/S0022112090000519>.
- [32] Huang NE, Chen DT, Tung C-C, Smith JR. Interactions between steady non-uniform currents and gravity waves with applications for current measurements. *J Phys Oceanogr* 1972;2(4):420–31. [http://dx.doi.org/10.1175/1520-0485\(1972\)002<0420:IBSWUC>2.0.CO;2](http://dx.doi.org/10.1175/1520-0485(1972)002<0420:IBSWUC>2.0.CO;2), URL [https://journals.ametsoc.org/view/journals/phoc/2/4/1520-0485\\_1972\\_002\\_0420\\_ibswuc\\_2\\_0\\_co\\_2.xml](https://journals.ametsoc.org/view/journals/phoc/2/4/1520-0485_1972_002_0420_ibswuc_2_0_co_2.xml).
- [33] Draycott S, Sellar B, Davey T, Noble D, Venugopal V, Ingram D. Capture and simulation of the ocean environment for offshore renewable energy. *Renew Sustain Energy Rev* 2019;104:15–29. <http://dx.doi.org/10.1016/j.rser.2019.01.011>, URL <https://www.sciencedirect.com/science/article/pii/S1364032119300115>.
- [34] Draycott S, Noble D, Davey T, Bruce T, Ingram D, Johanning L, Smith H, Day A, Kaklis P. Re-creation of site-specific multi-directional waves with non-collinear current. *Ocean Eng* 2018;152:391–403. <http://dx.doi.org/10.1016/j.oceaneng.2017.10.047>, URL <https://www.sciencedirect.com/science/article/pii/S0029801817306595>.
- [35] Hashemi MR, Grilli ST, Neill SP. A simplified method to estimate tidal current effects on the ocean wave power resource. *Renew Energy* 2016;96:257–69. <http://dx.doi.org/10.1016/j.renene.2016.04.073>, URL <https://www.sciencedirect.com/science/article/pii/S0960148116303755>.
- [36] Shi X, Li S, Liang B, Zhao J, Liu Y, Wang Z. Numerical study on the impact of wave-current interaction on wave energy resource assessments in Zhoushan sea area, China. *Renew Energy* 2023;215:119017. <http://dx.doi.org/10.1016/j.renene.2023.119017>, URL <https://www.sciencedirect.com/science/article/pii/S096014812300931X>.
- [37] Guo B, Wang T, Jin S, Duan S, Yang K, Zhao Y. A review of point absorber wave energy converters. *J Mar Sci Eng* 2022;10(10). <http://dx.doi.org/10.3390/jmse10101534>, URL <https://www.mdpi.com/2077-1312/10/10/1534>.
- [38] Silva L, Cazzolato B, Sergienco N, Ding B. Nonlinear dynamics of a floating offshore wind turbine platform via statistical quadratization — Mooring, wave and current interaction. *Ocean Eng* 2021;236:109471. <http://dx.doi.org/10.1016/j.oceaneng.2021.109471>, URL <https://www.sciencedirect.com/science/article/pii/S0029801821008738>.
- [39] Qu X, Li Y, Tang Y, Hu Z, Zhang P, Yin T. Dynamic response of spar-type floating offshore wind turbine in freak wave considering the wave-current interaction effect. *Appl Ocean Res* 2020;100:102178. <http://dx.doi.org/10.1016/j.apor.2020.102178>, URL <https://www.sciencedirect.com/science/article/pii/S0141118719311010>.
- [40] Coe RG, Yu Y-H, Van Rij J. A survey of WEC reliability, survival and design practices. *Energies* 2018;11(1). <http://dx.doi.org/10.3390/en11010004>, URL <https://www.scopus.com/inward/record.uri?eid=2-s2.0-85040626140&doi=10.3390%2fen11010004&partnerID=40&md5=5352ca98616155f8808bac8262cea465>.
- [41] Ropero-Giralda P, Crespo AJ, Tagliaferro B, Altomare C, Domínguez JM, Gómez-Gesteira M, Viccione G. Efficiency and survivability analysis of a point-absorber wave energy converter using DualSPHysics. *Renew Energy* 2020;162:1763–76. <http://dx.doi.org/10.1016/j.renene.2020.10.012>, URL <http://www.sciencedirect.com/science/article/pii/S0960148120315780>.
- [42] Tagliaferro B, Martínez-Estévez I, Domínguez JM, Crespo AJ, Götteman M, Engström J, Gómez-Gesteira M. A numerical study of a taut-moored point-absorber wave energy converter with a linear power take-off system under extreme wave conditions. *Appl Energy* 2022;311:118629. <http://dx.doi.org/10.1016/j.apenergy.2022.118629>, URL <https://www.sciencedirect.com/science/article/pii/S0306261922000988>.
- [43] Quartier N, Ropero-Giralda P, M. Domínguez J, Stratigaki V, Troch P. Influence of the drag force on the average absorbed power of heaving wave energy converters using smoothed particle hydrodynamics. *Water* 2021;13(3). <http://dx.doi.org/10.3390/w13030384>, URL <https://www.mdpi.com/2073-4441/13/3/384>.
- [44] Chen W, Dolgunteva I, Savin A, Zhang Y, Li W, Svensson O, Leijon M. Numerical modelling of a point-absorbing wave energy converter in irregular and extreme waves. *Appl Ocean Res* 2017;63:90–105. <http://dx.doi.org/10.1016/j.apor.2017.01.004>, URL <https://www.sciencedirect.com/science/article/pii/S0141118716302668>.
- [45] Sjökvist L, Wu J, Ransley E, Engström J, Eriksson M, Götteman M. Numerical models for the motion and forces of point-absorbing wave energy converters in extreme waves. *Ocean Eng* 2017;145:1–14. <http://dx.doi.org/10.1016/j.oceaneng.2017.08.061>, URL <https://www.sciencedirect.com/science/article/pii/S002980181730505X>.
- [46] Katsidoniotaki E, Shahrooz Z, Eskilsson C, Palm J, Engström J, Götteman M. Validation of a CFD model for wave energy system dynamics in extreme waves. *Ocean Eng* 2023;268:113320. <http://dx.doi.org/10.1016/j.oceaneng.2022.113320>, URL <https://www.sciencedirect.com/science/article/pii/S0029801822026038>.
- [47] Katsidoniotaki E, Götteman M. Numerical modeling of extreme wave interaction with point-absorber using OpenFOAM. *Ocean Eng* 2022;245:110268. <http://dx.doi.org/10.1016/j.oceaneng.2021.110268>, URL <https://www.sciencedirect.com/science/article/pii/S0029801821015754>.
- [48] Kumar A, Hayatdavoodi M. Effect of currents on nonlinear waves in shallow water. *Coast Eng* 2023;181:104278. <http://dx.doi.org/10.1016/j.coastaleng.2023.104278>, URL <https://www.sciencedirect.com/science/article/pii/S0378383923000029>.
- [49] Umeyama M. Coupled PIV and PTV measurements of particle velocities and trajectories for surface waves following a steady current. *J Waterw Port Coast Ocean Eng* 2011;137(2):85–94. [http://dx.doi.org/10.1061/\(ASCE\)WW.1943-5460.0000067](http://dx.doi.org/10.1061/(ASCE)WW.1943-5460.0000067).
- [50] Silva M, Vitola M, Esperança P, Sphaier S, Levi C. Numerical simulations of wave–current flow in an ocean basin. *Appl Ocean Res* 2016;61:32–41. <http://dx.doi.org/10.1016/j.apor.2016.10.005>, URL <https://www.sciencedirect.com/science/article/pii/S0141118716304345>.
- [51] Oliveira D, Lopes de Almeida J, Santiago A, Rigueiro C. Development of a CFD-based numerical wave tank of a novel multipurpose wave energy converter. *Renew Energy* 2022;199:226–45. <http://dx.doi.org/10.1016/j.renene.2022.08.103>, URL <https://www.scopus.com/inward/record.uri?eid=2-s2.0-85137684867&doi=10.1016%2fj.renene.2022.08.103&partnerID=40&md5=3340a68c8cb9a94d7eb7295fd89b524c>.
- [52] Kim S-Y, Kim K-M, Park J-C, Jeon G-M, Chun H-H. Numerical simulation of wave and current interaction with a fixed offshore substructure. *Int J Nav Archit Ocean Eng* 2016;8(2):188–97. <http://dx.doi.org/10.1016/j.ijnaoe.2016.02.002>, URL <https://www.sciencedirect.com/science/article/pii/S2092678216000285>.
- [53] Li Q, Wang J, Yan S, Gong J, Ma Q. A zonal hybrid approach coupling FNPt with OpenFOAM for modelling wave-structure interactions with action of current. *Ocean Syst Eng* 2018;8(4):381–407. <http://dx.doi.org/10.12989/ose.2018.8.4.381>, URL <https://www.scopus.com/inward/record.uri?eid=2-s2.0-85059274124&doi=10.12989%2fose.2018.8.4.381&partnerID=40&md5=1ca066da86b9aaf1b145515877be4ed6>.
- [54] Violeau D, Rogers B. Smoothed particle hydrodynamics (SPH) for free-surface flows: past, present and future. *J Hydraul Res* 2016;54(1):1–26. <http://dx.doi.org/10.1080/00221686.2015.1119209>.
- [55] Lind SJ, Rogers BD, Stansby PK. Review of smoothed particle hydrodynamics: Towards converged Lagrangian flow modelling: Smoothed particle hydrodynamics review. *Proc R Soc Lond Ser A Math Phys Sci* 2020;476(2241). <http://dx.doi.org/10.1098/rspa.2019.0801>, URL <https://www.scopus.com/inward/record.uri?eid=2-s2.0-85093071840&doi=10.1098%2frspa.2019.0801&partnerID=40&md5=89acbe0b6ee7467cc93577d1231fe658>.
- [56] He M, Gao X-f, Xu W-h. Numerical simulation of wave-current interaction using the SPH method. *J Hydrodyn* 2018;30:535–8. <http://dx.doi.org/10.1007/s42241-018-0042-5>.
- [57] Ni X-y, Feng W-b, Huang S-c, Hu Z-j, Liu Y. An SPH wave-current flume using open boundary conditions. *J Hydrodyn* 2020;32:537–47.
- [58] Yang Y, Draycott S, Stansby PK, Rogers BD. A numerical flume for waves on variable sheared currents using smoothed particle hydrodynamics (SPH) with open boundaries. *Appl Ocean Res* 2023;135:103527. <http://dx.doi.org/10.1016/j.apor.2023.103527>, URL <https://www.sciencedirect.com/science/article/pii/S0141118723000688>.
- [59] Yang Y, Stansby PK, Rogers BD, Buldakov E, Stagonas D, Draycott S. The loading on a vertical cylinder in steep and breaking waves on sheared currents using smoothed particle hydrodynamics. *Phys Fluids* 2023;35(8).

- <http://dx.doi.org/10.1063/5.0160021>, URL <https://www.scopus.com/inward/record.uri?eid=2-s2.0-85169792037&doi=10.1063%2F5.0160021&partnerID=40&md5=f1745836c17fe9351e40af52711fd34c>.
- [60] Zhang F, Crespo A, Altomare C, Domínguez J, Marzeddu A, Shang S-p, Gómez-Gesteira M. DualSPHysics: A numerical tool to simulate real breakwaters. *J Hydrodyn* 2018;30. <http://dx.doi.org/10.1007/s42241-018-0010-0>.
- [61] Domínguez JM, Fourtakas G, Altomare C, Canelas RB, Tafuni A, García-Feal O, Martínez-Estévez I, Mokos A, Vacondio R, Crespo AJC, Rogers BD, Stansby PK, Gómez-Gesteira M. DualSPHysics: from fluid dynamics to multiphysics problems. *Comput Part Mech* 2022;9(5):867–95. <http://dx.doi.org/10.1007/s40571-021-00404-2>.
- [62] Roper-Giralda P, Crespo AJC, Coe RG, Tagliaferro B, Domínguez JM, Bacelli G, Gómez-Gesteira M. Modelling a heaving point-absorber with a closed-loop control system using the DualSPHysics code. *Energies* 2021;14(3):760. <http://dx.doi.org/10.3390/en14030760>, URL <https://www.mdpi.com/1996-1073/14/3/760>. Number: 3 Publisher: Multidisciplinary Digital Publishing Institute.
- [63] Crespo A, Tagliaferro B, Martínez-Estévez I, Domínguez JM, deCastro M, Gómez-Gesteira M, Altomare C, Brito M, Bernardo F, Ferreira RM, Capasso S, Viccione G, Quartier N, Stratigaki V, Troch P, Simonetti I, Cappietti L, Götteman M, Engström J, Clemente D, Rosa-Santos P, Taveira-Pinto F, Bacelli G, Coe R, Fourtakas G, Rogers B, Stansby P. On the state-of-the-art of CFD simulations for wave energy converters within the open-source numerical framework of DualSPHysics. *Proc Eur Wave Tidal Energy Conf* 2023;15. <http://dx.doi.org/10.36688/ewtec-2023-145>, URL <https://submissions.ewtec.org/proc-ewtec/article/view/145>.
- [64] Tagliaferro B, Karimirad M, Martínez-Estévez I, Domínguez JM, Viccione G, Crespo AJC. Numerical assessment of a tension-leg platform wind turbine in intermediate water using the smoothed particle hydrodynamics method. *Energies* 2022;15(11). <http://dx.doi.org/10.3390/en15113993>, URL <https://www.mdpi.com/1996-1073/15/11/3993>.
- [65] Tagliaferro B, Karimirad M, Altomare C, Götteman M, Martínez-Estévez I, Capasso S, Domínguez JM, Viccione G, Gómez-Gesteira M, Crespo AJ. Numerical validations and investigation of a semi-submersible floating offshore wind turbine platform interacting with ocean waves using an SPH framework. *Appl Ocean Res* 2023;141. <http://dx.doi.org/10.1016/j.apor.2023.103757>, URL <https://www.scopus.com/inward/record.uri?eid=2-s2.0-85174624401&doi=10.1016%2Fj.apor.2023.103757&partnerID=40&md5=4cabe6e7916e15016b2c73372f4ecfe9>.
- [66] Tagliaferro B, Karimirad M, Capasso S, Götteman M, Martínez-Estévez I, Domínguez JM, Altomare C, Viccione G, Crespo AJ, Negrut D. Coupled numerical simulation of floating offshore wind turbine platforms: investigating the effects of wave and wind loading using a high-fidelity sph-based model. *American Society of Mechanical Engineers (ASME)*; 2023. <http://dx.doi.org/10.1115/1.6107232>, URL <https://www.scopus.com/inward/record.uri?eid=2-s2.0-85185220402&doi=10.1115%2F1.6107232-1196348&partnerID=40&md5=bc86e57906aca9ce89cb5b0a1905565>.
- [67] Tan Z, Sun P-N, Liu N-N, Li Z, Lyu H-G, Zhu R-H. SPH simulation and experimental validation of the dynamic response of floating offshore wind turbines in waves. *Renew Energy* 2023;205:393–409. <http://dx.doi.org/10.1016/j.renene.2023.01.081>, URL <https://www.sciencedirect.com/science/article/pii/S0960148123000903>.
- [68] Domínguez JM, Crespo AJ, Gómez-Gesteira M. Optimization strategies for CPU and GPU implementations of a smoothed particle hydrodynamics method. *Comput Phys Comm* 2013;184(3):617–27. <http://dx.doi.org/10.1016/j.cpc.2012.10.015>, URL <https://www.sciencedirect.com/science/article/pii/S001046551200358X>.
- [69] Tasora A, Serban R, Mazhar H, Pazouki A, Melanz D, Fleischmann J, Taylor M, Sugiyama H, Negrut D. Chrono: An open source multi-physics dynamics engine. 2016, p. 19–49. [http://dx.doi.org/10.1007/978-3-319-40361-8\\_2](http://dx.doi.org/10.1007/978-3-319-40361-8_2).
- [70] Martínez-Estévez I, Domínguez JM, Tagliaferro B, Canelas RB, García-Feal O, Crespo AJC, Gómez-Gesteira M. Coupling of an SPH-based solver with a multiphysics library. *Comput Phys Comm* 2023;283:108581. <http://dx.doi.org/10.1016/j.cpc.2022.108581>, URL <https://www.sciencedirect.com/science/article/pii/S0010465522003009>.
- [71] Hall M. MoorDyn user's guide. 2021, <http://www.matt-hall.ca/moordyn.html>. (Accessed 27 December 2021).
- [72] Domínguez J, Crespo A, Hall M, Altomare C, Wu M, Stratigaki V, Troch P, Cappietti L, Gómez-Gesteira M. SPH simulation of floating structures with moorings. *Coast Eng* 2019;153:103560. <http://dx.doi.org/10.1016/j.coastaleng.2019.103560>.
- [73] Mitsui J, Altomare C, Crespo AJ, Domínguez JM, Martínez-Estévez I, Suzuki T, Kubota S, Gómez-Gesteira M. DualSPHysics modelling to analyse the response of tetrapods against solitary wave. *Coast Eng* 2023;183:104315. <http://dx.doi.org/10.1016/j.coastaleng.2023.104315>, URL <https://www.sciencedirect.com/science/article/pii/S037838392300039X>.
- [74] Tafuni A, Domínguez J, Vacondio R, Crespo A. A versatile algorithm for the treatment of open boundary conditions in smoothed particle hydrodynamics GPU models. *Comput Methods Appl Mech Engrg* 2018;342. <http://dx.doi.org/10.1016/j.cma.2018.08.004>.
- [75] Ruffini G, Domínguez J, Briganti R, Altomare C, Stolle J, Crespo A, Ghiassi B, Capasso S, De Girolamo P. MESH-IN: A MESHed INlet offline coupling method for 3-D extreme hydrodynamic events in DualSPHysics. *Ocean Eng* 2023;268. <http://dx.doi.org/10.1016/j.oceaneng.2022.113400>.
- [76] Altomare C, Tagliaferro B, Domínguez JM, Suzuki T, Viccione G. Improved relaxation zone method in SPH-based model for coastal engineering applications. *Appl Ocean Res* 2018;81:15–33. <http://dx.doi.org/10.1016/j.apor.2018.09.013>, URL <https://www.sciencedirect.com/science/article/pii/S0141118718303705>.
- [77] Waters R, Stålberg M, Danielsson O, Svensson O, Gustafsson S, Strömstedt E, Eriksson M, Sundberg J, Leijon M. Experimental results from sea trials of an offshore wave energy system. *Appl Phys Lett* 2007;90(3):034105. <http://dx.doi.org/10.1063/1.2432168>.
- [78] Götteman M, Engström J, Eriksson M, Hann M, Ransley E, Greaves D, Leijon M. Wave loads on a point-absorbing wave energy device in extreme waves. *International ocean and polar engineering conference, vol. All Days, 2015, ISOPE I-15-593*.
- [79] DNVGL-ST-0437. *Loads and site conditions for wind turbines*. Standard, Oslo, NO: DNV-GL; 2016.
- [80] Gotthardt H, Khayyer A, Shimizu Y. Entirely Lagrangian meshfree computational methods for hydroelastic fluid-structure interactions in ocean engineering—Reliability, adaptivity and generality. *Appl Ocean Res* 2021;115:102822. <http://dx.doi.org/10.1016/j.apor.2021.102822>, URL <https://www.sciencedirect.com/science/article/pii/S0141118721002959>.
- [81] Liu G, Liu M. *Smoothed particle hydrodynamics*. World scientific; 2003. <http://dx.doi.org/10.1142/5340>.
- [82] Liu G. *Meshfree methods: moving beyond the finite element method*. CRC Press; 2009.
- [83] Monaghan J. Smoothed particle hydrodynamics. *Annu Rev Astron Astrophys* 1992;30(1):543–74. <http://dx.doi.org/10.1146/annurev.aa.30.090192.002551>.
- [84] Wendland H. Piecewise polynomial, positive definite and compactly supported radial basis functions of minimal degree. *Adv Comput Math* 1995;4(1):389–96. <http://dx.doi.org/10.1007/BF02123482>, URL <http://sro.sussex.ac.uk/id/eprint/24323/>.
- [85] Fourtakas G, Domínguez JM, Vacondio R, Rogers BD. Local uniform stencil (LUST) boundary condition for arbitrary 3-D boundaries in parallel smoothed particle hydrodynamics (SPH) models. *Comput & Fluids* 2019;190:346–61. <http://dx.doi.org/10.1016/j.complfluid.2019.06.009>.
- [86] Molteni D, Colagrossi A. A simple procedure to improve the pressure evaluation in hydrodynamic context using the SPH. *Comput Phys Comm* 2009;180(6):861–72. <http://dx.doi.org/10.1016/j.cpc.2008.12.004>.
- [87] Antuono M, Colagrossi A, Marrone S. Numerical diffusive terms in weakly-compressible SPH schemes. *Comput Phys Comm* 2012;183(12):2570–80. <http://dx.doi.org/10.1016/j.cpc.2012.07.006>, URL <http://www.sciencedirect.com/science/article/pii/S0010465512002342>.
- [88] Leimkuhler B, Reich S, Zentrum K, Str H, Skeel R. *Integration methods for molecular dynamics*. Vol. 82, 1995, [http://dx.doi.org/10.1007/978-1-4612-4066-2\\_10](http://dx.doi.org/10.1007/978-1-4612-4066-2_10).
- [89] Monaghan J, Kos A, Issa N. Fluid motion generated by impact. *J Waterw Port Coast Ocean Eng* 2003;129(6):250–9. [http://dx.doi.org/10.1061/\(ASCE\)0733-950X\(2003\)129:6\(250\)](http://dx.doi.org/10.1061/(ASCE)0733-950X(2003)129:6(250)).
- [90] Canelas RB, Domínguez JM, Crespo AJ, Gómez-Gesteira M, Ferreira RM. A smooth particle hydrodynamics discretization for the modelling of free surface flows and rigid body dynamics. *Internat J Numer Methods Fluids* 2015;78(9):581–93. <http://dx.doi.org/10.1002/fld.4031>.
- [91] English A, Domínguez J, Vacondio R, Crespo A, Stansby P, Lind S, Chiapponi I, Gómez-Gesteira M. Modified dynamic boundary conditions (mDBC) for general-purpose smoothed particle hydrodynamics (SPH): application to tank sloshing, dam break and fish pass problems. *Comput Part Mech* 2022;9(5):1–15. <http://dx.doi.org/10.1007/s40571-021-00403-3>, URL <https://www.scopus.com/inward/record.uri?eid=2-s2.0-85103385297&doi=10.1007%2Fs40571-021-00403-3&partnerID=40&md5=9c42490a240326320537466675df4c27>.
- [92] Crespo A, Gómez-Gesteira M, Dalrymple R. Boundary conditions generated by dynamic particles in SPH methods. *Comput Mater Contin* 2007;5(3):173–84.
- [93] Zhang F, Crespo A, Altomare C, Domínguez J, Marzeddu A, Shang S-p, Gómez-Gesteira M. DualSPHysics: A numerical tool to simulate real breakwaters. *J Hydrodyn* 2018;30. <http://dx.doi.org/10.1007/s42241-018-0010-0>.
- [94] Liu M, Liu G. Restoring particle consistency in smoothed particle hydrodynamics. *Appl Numer Math* 2006;56(1):19–36. <http://dx.doi.org/10.1016/j.apnum.2005.02.012>, URL <https://www.sciencedirect.com/science/article/pii/S0168927405000565>.
- [95] Domínguez J, Crespo A, Fourtakas G et al. Evaluation of reliability and efficiency of different boundary conditions in an SPH code. In: *Proceedings of the 10th international SPHERIC workshop*. 2015, p. 341–8.
- [96] Capasso S, Tagliaferro B, Güzel H, Yilmaz A, Dal K, Kocaman S, Viccione G, Evangelista S. A numerical validation of 3D experimental dam-break wave interaction with a sharp obstacle using DualSPHysics. *Water* 2021;13(15). <http://dx.doi.org/10.3390/w13152133>.
- [97] Brito M, Bernardo F, Neves MG, Neves DRBC, Crespo AJC, Domínguez JM. Numerical model of constrained wave energy hyperbaric converter under full-scale sea wave conditions. *J Mar Sci Eng* 2022;10(10). <http://dx.doi.org/10.3390/jmse10101489>, URL <https://www.mdpi.com/2077-1312/10/10/1489>.

- [98] Martínez-Estévez I, Tagliaferro B, El Rahi J, Domínguez J, Crespo A, Troch P, Gómez-Gesteira M. Coupling an SPH-based solver with an FEA structural solver to simulate free surface flows interacting with flexible structures. *Comput Methods Appl Mech Engrg* 2023;410:115989. <http://dx.doi.org/10.1016/j.cma.2023.115989>, URL <https://www.sciencedirect.com/science/article/pii/S0045782523001123>.
- [99] Ruffini G, Briganti R, De Girolamo P, Stolle J, Ghiassi B, Castellino M. Numerical modelling of flow-debris interaction during extreme hydrodynamic events with DualSPHysics-Chrono. *Appl Sci* 2021;11(8). <http://dx.doi.org/10.3390/app11083618>, URL <https://www.mdpi.com/2076-3417/11/8/3618>.
- [100] Marrone S, Colagrossi A, Antuono M, Colicchio G, Graziani G. An accurate SPH modeling of viscous flows around bodies at low and moderate Reynolds numbers. *J Comput Phys* 2013;245:456–75. <http://dx.doi.org/10.1016/j.jcp.2013.03.011>, URL <https://www.sciencedirect.com/science/article/pii/S0021999113001885>.
- [101] Verbrugge T, Domínguez J, Altomare C, Tafuni A, Vacondio R, Troch P, Kortenhaus A. Non-linear wave generation and absorption using open boundaries within DualSPHysics. *Comput Phys Comm* 2019;240:46–59. <http://dx.doi.org/10.1016/j.cpc.2019.02.003>.
- [102] Verbrugge T, Stratigaki V, Altomare C, Domínguez J, Troch P, Kortenhaus A. Implementation of open boundaries within a two-way coupled SPH model to simulate nonlinear wave–structure interactions. *Energies* 2019;12(4). <http://dx.doi.org/10.3390/en12040697>.
- [103] Capasso S, Tagliaferro B, Mancini S, Martínez-Estévez I, Altomare C, Domínguez JM, Viccione G. Regular wave seakeeping analysis of a planing hull by smoothed particle hydrodynamics: A comprehensive validation. *J Mar Sci Eng* 2023;11(4). <http://dx.doi.org/10.3390/jmse11040700>, URL <https://www.mdpi.com/2077-1312/11/4/700>.
- [104] Capasso S, Tagliaferro B, González-Ávalos R, Martínez-Estévez I, Domínguez JM, Altomare C, Crespo AJ, Viccione G. Numerical simulation of a moored wave-buoy in waves and current by smoothed particle hydrodynamics. Vol. 7, 2023, <http://dx.doi.org/10.1115/OMAE2023-105023>, URL <https://www.scopus.com/inward/record.uri?eid=2-s2.0-85169785559&doi=10.1115%2fOMAE2023-105023&partnerID=40&md5=6c81f79473f5224f6237e955ea6d808>.
- [105] Canelas R, Brito M, Feal O, Domínguez J, Crespo A. Extending DualSPHysics with a differential variational inequality: modeling fluid–mechanism interaction. *Appl Ocean Res* 2018;76:88–97. <http://dx.doi.org/10.1016/j.apor.2018.04.015>.
- [106] Machado M, Moreira P, Flores P, Lankarani HM. Compliant contact force models in multibody dynamics: Evolution of the hertz contact theory. *Mech Mach Theory* 2012;53:99–121. <http://dx.doi.org/10.1016/j.mechmachtheory.2012.02.010>, URL <https://www.sciencedirect.com/science/article/pii/S0094114X1200047X>.
- [107] Martínez-Estévez I. MoorDynPlus. 2021, <https://github.com/imestevez/MoorDynPlus>. [Accessed 27 July 2021].
- [108] Holthuijsen LH. *Waves in oceanic and coastal waters*. Cambridge University Press; 2010.
- [109] Saruwatari A, Ingram DM, Cradden L. Wave–current interaction effects on marine energy converters. *Ocean Eng* 2013;73:106–18. <http://dx.doi.org/10.1016/j.oceaneng.2013.09.002>, URL <https://www.sciencedirect.com/science/article/pii/S0029801813003454>.
- [110] Warren I, Bach H. MIKE 21: a modelling system for estuaries, coastal waters and seas. *Environ Softw* 1992;7(4):229–40. [http://dx.doi.org/10.1016/0266-9838\(92\)90006-P](http://dx.doi.org/10.1016/0266-9838(92)90006-P), URL <https://www.sciencedirect.com/science/article/pii/026698389290006P>. 3rd International Software Exhibition for Environmental Science and Engineering.
- [111] Booij N, Ris R, Holthuijsen L. A third-generation wave model for coastal regions, part I, model description and validation. *J Geophys Res* 1999;104:7649–56.
- [112] Fenton JD. A fifth-order Stokes theory for steady waves. *J Waterw Port Coast Ocean Eng* 1985;111(2):216–34. [http://dx.doi.org/10.1061/\(ASCE\)0733-950X\(1985\)111:2\(216\)](http://dx.doi.org/10.1061/(ASCE)0733-950X(1985)111:2(216)), URL <https://ascelibrary.org/doi/abs/10.1061/%28ASCE%290733-950X%281985%2911%3A2%28216%29>.
- [113] Gomez-Gesteira M, Rogers B, Crespo A, Dalrymple R, Narayanaswamy M, Domínguez J. Sphysics - development of a free-surface fluid solver - part 1: Theory and formulations. *Comput Geosci* 2012;48:289–99. <http://dx.doi.org/10.1016/j.cageo.2012.02.029>.
- [114] Altomare C, Tagliaferro B, Domínguez J, Suzuki T, Viccione G. Improved relaxation zone method in SPH-based model for coastal engineering applications. *Appl Ocean Res* 2018;81:15–33. <http://dx.doi.org/10.1016/j.apor.2018.09.013>, URL <https://www.sciencedirect.com/science/article/pii/S0141118718303705>.
- [115] Noble DR, Davey TA, Smith HC, Kaklis P, Robinson A, Bruce T. Spatial variation in currents generated in the FloWave ocean energy research facility. In: *Proceedings of the 11th European wave and tidal energy conference. EWTEC2015, Nantes France; 2015*, p. 1–8.
- [116] Hedges T. Regions of validity of analytical wave theories. *Proc Ice Water Maritime Energy* 1995;112:111–4. <http://dx.doi.org/10.1680/iwtme.1995.27656>.
- [117] Altomare C, Domínguez J, Crespo A, González-Cao J, Suzuki T, Gómez-Gesteira M, Troch P. Long-crested wave generation and absorption for SPH-based DualSPHysics model. *Coast Eng* 2017;127:37–54. <http://dx.doi.org/10.1016/j.coastaleng.2017.06.004>.
- [118] Rota Roselli RA, Vernengo G, Altomare C, Brizzolara S, Bonfiglio L, Guercio R. Ensuring numerical stability of wave propagation by tuning model parameters using genetic algorithms and response surface methods. *Environ Model Softw* 2018;103:62–73. <http://dx.doi.org/10.1016/j.envsoft.2018.02.003>.
- [119] Sørsum SH, Fonseca N, Kent M, Faria RP. Assessment of nylon versus polyester ropes for mooring of floating wind turbines. *Ocean Eng* 2023;278:114339. <http://dx.doi.org/10.1016/j.oceaneng.2023.114339>, URL <https://www.sciencedirect.com/science/article/pii/S0029801823007230>.
- [120] Giannini G, Temiz I, Rosa-Santos P, roozi Z, Ramos V, Götteman M, Engström J, Day S, Taveira-Pinto F. Wave energy converter power take-off system scaling and physical modelling. *J Mar Sci Eng* 2020;8(9). <http://dx.doi.org/10.3390/jmse8090632>, URL <https://www.mdpi.com/2077-1312/8/9/632>.
- [121] Engström J, Sjökvist L, Götteman M, Eriksson M, Hann M, Ransley E, Greaves D, Leijon M. Buoy geometry and its influence on survivability for a point absorbing wave energy converter: Scale experiment and CFD simulations. In: *Proc. of the in marine energy technology symposium, Washington DC, USA, 2017*. 2017, URL <http://hdl.handle.net/10026.1/13620>.
- [122] DNV-RP-C205. *Recommended practice: environmental conditions and environmental loads*. DNV; 2014.
- [123] Götteman M. Multiple cluster scattering with applications to wave energy park optimizations. *Appl Ocean Res* 2022;125. <http://dx.doi.org/10.1016/j.apor.2022.103256>.
- [124] Klise K, Pauly R, Ruehl KM, Olson S, Shippert T, Morrell Z, Bredin S, Lansing C, Macduff M, Martin T, Sivaraman C, Gunawan B, Driscoll F. MhKit (marine and hydrokinetic toolkit) - python. 2020, <http://dx.doi.org/10.5281/zenodo.3924683>, [Computer Software].
- [125] Eckert-Gallup AC, Sallaberry CJ, Dallman AR, Neary VS. Application of principal component analysis (PCA) and improved joint probability distributions to the inverse first-order reliability method (I-FORM) for predicting extreme sea states. *Ocean Eng* 2016;112:307–19. <http://dx.doi.org/10.1016/j.oceaneng.2015.12.018>, URL <https://www.sciencedirect.com/science/article/pii/S0029801815006721>.
- [126] Hedges T, Lee B. The equivalent uniform current in wave-current computations. *Coast Eng* 1992;16(3):301–11.
- [127] Götteman M, Giassi M, Engström J, Isberg J. Advances and challenges in wave energy park optimization—A review. *Front Energy Res* 2020;8:26. <http://dx.doi.org/10.3389/fenrg.2020.00026>, URL <https://www.frontiersin.org/article/10.3389/fenrg.2020.00026>.
- [128] Quartier N, Vervaeet T, Fernandez GV, Domínguez JM, Crespo AJ, Stratigaki V, Troch P. High-fidelity numerical modelling of a two-WEC array with accurate implementation of the PTO system and control strategy using DualSPHysics. *Energy* 2024;296. <http://dx.doi.org/10.1016/j.energy.2024.130888>, URL <https://www.scopus.com/inward/record.uri?eid=2-s2.0-85189753193&doi=10.1016%2fj.energy.2024.130888&partnerID=40&md5=5781494604cb84ba331e759f3c50e32c>. Cited by: 0.
- [129] Stavropoulou C, Goude A, Katsidoniotaki E, Götteman M. Fast time-domain model for the preliminary design of a wave power farm. *Renew Energy* 2023;219:119482. <http://dx.doi.org/10.1016/j.renene.2023.119482>, URL <https://www.sciencedirect.com/science/article/pii/S0960148123013976>.
- [130] Meyer J, Windt C, Hildebrandt A, Schlurmann T. Mechanically coupled wave farms: On the accuracy of a mid-fidelity hydrodynamic model under consideration of varying calibration approaches. *Ocean Eng* 2024;305:117874. <http://dx.doi.org/10.1016/j.oceaneng.2024.117874>, URL <https://www.sciencedirect.com/science/article/pii/S0029801824012125>.
- [131] Capasso S, Tagliaferro B, Martínez-Estévez I, Domínguez JM, Crespo AJC, Viccione G. A DEM approach for simulating flexible beam elements with the Project Chrono core module in DualSPHysics. *Comput Part Mech* 2022;9(5):969–85. <http://dx.doi.org/10.1007/s40571-021-00451-9>.
- [132] O'Connor J, Rogers BD. A fluid–structure interaction model for free-surface flows and flexible structures using smoothed particle hydrodynamics on a GPU. *J Fluids Struct* 2021;104:103312. <http://dx.doi.org/10.1016/j.jfluidstruct.2021.103312>, URL <https://www.sciencedirect.com/science/article/pii/S0889974621000955>.
- [133] Jonsson IG, Arneborg L. Energy properties and shoaling of higher-order stokes waves on a current. *Ocean Eng* 1995;22(8):819–57. [http://dx.doi.org/10.1016/0029-8018\(95\)00008-9](http://dx.doi.org/10.1016/0029-8018(95)00008-9), URL <https://www.sciencedirect.com/science/article/pii/0029801895000089>.